Orbit Calculations for Determination of Heavy Ion Beam Probe Ports on W7X

A. Teubel
Max-Planck-Institut für Plasmaphysik
D-85748 Garching, Germany

IPP III/214 November 1996

MAX-PLANCK-INSTITUT FÜR PLASMAPHYSIK

85748 GARCHING BEI MÜNCHEN

MAX-PLANCK-INSTITUT FÜR PLASMAPHYSIK
GARCHING BEI MÜNCHEN

Orbit Calculations for Determination of Heavy Ion Beam Probe Ports on W7X

A. Teubel
Max-Planck-Institut für Plasmaphysik
D-85748 Garching, Germany

IPP III/214 November 1996

Die nachstehende Arbeit wurde im Rahmen des Vertrages zwischen dem Max-Planck-Institut für Plasmaphysik und der Europäischen Atomgemeinschaft über die Zusammenarbeit auf dem Gebiete der Plasmaphysik durchgeführt.

Abstract

The heavy ion beam probe (HIBP) is an unique technique in fusion experiments for direct measurements of plasma electric potential. By orbit calculations the port geometry of the injection and diagnostic ports has been determined for the W7-X stellerator project. An optimisation with respect to best access, minimum necessary beam energy and maximum detectable plasma region has been performed. As result three different locations for HIBP were found. Because of other diagnostics and heating systems already fixed on ports, the most favourable scenario for HIBP is given by an injection at 15° and detection at 22° in toroidal direction. The energy necessary to detect the plasma centre corresponds to the existing TEXT/UG diagnostic (2MeV Tl^+ ions).

1. Introduction

The heavy ion beam probe (HIBP) is a unique tool for research in magnetic fusion experiments. Starting in the sixties with an arc discharge at a small facility [1] it is now a powerful diagnostic (Table 1) on tokamaks (2MeV at TEXT/UG) and helical systems (6MeV LHD-project). So far HIBP is the only method for direct measurement of the electric potential ($\Phi(r)$) without perturbations of the plasma. Additionally the diagnostic is used for determination of electron density ($n_e(r)$) and temperature ($T_e(r)$), poloidal magnetic field ($B_{pol}(r)$) and plasma current ($I_{pla}(r)$) as well as the electrostatically induced particle flux (Γ). Fluctuations and cross-correlations of most of these quantities has been studied due to the high time and space resolution of HIBP [2-15].
The influence of an electric field on the neoclassical transport was discussed in [16]. On the other hand as well known from the beginning of experimental fusion research, the plasma loss process is much faster than the predictions based on binary collisions. The electric field is considered to play a key role in understanding this anomalous transport. For a detailed discussion of the influence of the electric field on the confinement via **B**x**E** rotation and via fluctuations see [17]. Thus it would be very useful to have such an important diagnostic even at the new stellerator projects W7-X and LHD. The design of the LHD/HIBP is in good progress [18-20] and the diagnostic will be realised in future.
The paper reports on orbit calculations for an HIBP on W7-X to decide if and in which geometry ports have to be taken into account for the W7X-engineering design. Mainly the problem of beam access to the plasma which is crucial for the modular stellerator was considered. In a first approach ports in different poloidal planes were determined as candidates for the injection and diagnostic parts.

2. Basic principles

Most commonly singly charged heavy ions (primaries) are injected across the magnetic field into the plasma. Passing the plasma doubly charged particles (secondaries) are produced by ionisation. The magnetic field will separate primaries from secondaries, which will be detected and analysed outside the plasma (Fig. 1). Knowing the **B**-field structure, beam energy, starting position and velocity direction of the primaries as well as the detection place of secondaries allows the calculation of the ionisation place **r**. Measuring the energy difference of primary and secondary particles gives the electric field potential via energy conservation law. Thus a $\Phi(r)$-profile can be obtained by changing the beam energy or the initial angle (Fig. 2). An approximated necessary criteria for secondaries reaching the detector plate and not being

confined is given by $r_L > a$ with r_L being the averaged Larmor radius and the minor plasma radius a , which yields

$$MW_b / q_s^2 > a^2 B^2 / 2$$

(W_b - beam energy, M - ion mass, q_s - secondaries charge, B - mean magnitude of magnetic field on axis).
The injection of neutrals and detection of singly charged ions was used in experiments, too [21, 22]. It has the advantage of better access of neutrals to the plasma (no curvature) and by a factor of 4 reduced required product MW_b.
On the other hand the advantages of singly charged particle injection are: lower beam attenuation, no need of neutralisation chamber and higher beam currents. Typical ions in present experiments/projects are Cs^+ (A=133), Tl^+ (A=203, 205) and Au^- (A=197).
There are two mechanisms caused by beam-plasma interaction affecting the use of HIBP. By ion-electron, ion-ion and charge-exchange collisions the beam intensity will be attenuated. At low energies the electron impact process dominates, whereas at higher energies ($W_b > 2$MeV) ion-ion collisions become important and contribute significantly. Beam attenuation can impose limitations on the operating regime of HIBP, especially for larger devices (a>0.3m) at high densities. E.g., in LHD at $n_e > 10^{20}m^{-3}$ a primary beam current of 10μA yields a 10^{-8}nA secondary one, which corresponds to about 3000/s particles. Present diagnostics would fail and therefore a new particle counting method is necessary (see Fig. 3). For a detailed discussion of cross sections and problems concerned with beam attenuation see [18, 23].
Multiple Coulomb collisions of heavy ions with plasma ions and electrons result in an energy slowing-down of beam particles. Whereas for present devices this effect can be neglected, for larger paths of trajectories inside the plasma (>1m) the energy attenuation has to be taken into account. As shown in [18, 19] for LHD at high densities and low temperatures the energy loss can reach some keV (Fig. 4), influencing less the beam trajectories but of course strongly the $\Phi(r)$ determination. Because of energy and intensity attenuation it seems hardly possible to realise potential fluctuations with HIBP at W7X and LHD with today's available techniques.

3. Diagnostic hardware

Schematics of a tokamak (TEXT) and a helical device (LHD) HIBP diagnostic configuration are shown in Figs. 5a and 5b. In both cases it consists of three main components [2-4].

1) The injection part includes the ion source, beam accelerator and a beam alignment/bending system. Important requirements on ion sources are low energy spread of heavy ions (<1eV), small beam width (<1cm), large ion currents (>10μA) and long life times (>100h in pulsed mode). Most commonly thermoionic sources are used. The accelerator (e.g., Van-de-Graaff type) should produce a high energy beam with small ripple ($<10^{-4}$)

2) A pair of sweep plates controls the injection angles of primaries and thus at fixed W_b the ionisation point. In stellerators with their inherent 3D **B**-field structure a second pair of electrostatic plates is installed to control the entrance angles into the energy analyser. A swing of the full voltage range (10kV/cm in 2MeV at TEXT/UG) within a few milliseconds is realised. The system has to be able to handle currents induced by UV-light from the plasma during operation as well as voltage breakdowns.

3) The third and most crucial component is the energy analyser with its amplifier unit. Mainly analysers have been optimised to measure equilibrium electrostatic potential profiles, which requires an accuracy of the ratio $\Delta W_b/W_b = 10^{-5}$. Proca-Green type parallel analysers [2, 25, 26] (Figs. 6a and 6b) are widely used. The beam enters through the entrance slit (left in Fig. 6a) and moves into a region of uniform electric field. There it is deflected downwards to the split plates in a field free region. The isolated plates (Fig. 6b) are electrically connected to the amplifier unit measuring the currents i_1 to i_4. The sum signal ($i_{sum}=i_1+i_2+i_3+i_4$) gives information about the electron density and the right-left ratio ($(i_1-i_2+i_3-i_4)/i_{sum}$) about the toroidal component of the magnetic vector potential [8]. Fixing the voltage V_A, the beam energy of secondaries can be determined via the measured currents by

$$W_{bs} = q_s V_A \, (G + F \, (i_1+i_2-i_3-i_4) \, / \, i_{sum})$$

where G and F being the "gain" and "offline" function, respectively, depending only on geometrical quantities. Thus the electrostatic potential is given by

$$\Phi = (W_{bs} - W_{bp})/(q_s - q_p).$$

To achieve high accurate measurements several problems have to be solved: non uniform electric fields, mechanical misalignment, stray magnetic fields, UV-light from plasma, high voltage effects and shielding against radiation. Cylindrical analysers [18, 27, 28] are able to work with much lower voltages in contrast to Proca-Green analysers and are therefore used on LHD/HIBP project. Other types of analysers applied in experiments are multiple cell detectors [4, 29, 30] and grid analysers [3]. A quite different technique based on the time of flight method is under discussion [31].

4. Orbit calculation and port geometry

4.1 Orbit calculations

To decide about the possibility of using HIBP at W7-X a 3D orbit FORTRAN-code was developed (based on a 2D C-code from CFN Lisbon) to determine the orbits of ions for different beam injection parameters (starting point and direction as well as energy). Without loss of generality Cs^+ was taken as primary ion species and according to preliminary studies W_b = 3MeV was fixed (3MeV Cs^+ corresponds to 2MeV Tl^+ at TEXT/UG).
The trajectory of a primary or secondary ion was calculated neglecting electrical fields by numerical integration of the equations:

$$\mathbf{dr/dt = v}$$
$$\mathbf{dv/dt} = (q_{s,b} / m_{Cs})\ (\mathbf{v} \times \mathbf{B}) .$$

The **B**-field was determined by the GOURDON code for the standard vacuum configuration. According to the planned standard operational regime at W7-X the mean magnetic field on the axis was fixed: $B_0 = 2.5T$.
Then the components (B_R, B_ϕ, B_z) stored on a 3D-mesh were taken as input for the orbit code. Additionally, the GOURDON code supplied for each mesh point the effective plasma radius r_{eff} and the minimum distance to the coil filaments, which allows later on an optimisation.
Fixing the distance from the mean magnetic axis (r_{m0}), the trajectory of a Cs-primary (W_b = 3MeV) is uniquely determined by 4 parameters - two space angles (θ_0 , Φ_0) and two velocity directions (θ_{v0}, Φ_{v0}) see Fig. 9. Trajectory points inside the plasma (r_{eff}<a=0.52m) were used to determine the corresponding orbits of secondaries. Varying these four parameters optimal ion trajectories can be found with respect to:
1) maximum distance of the primary to the coil filaments,
2) primary should reach a minimum r_{eff} and
3) maximum distance of secondaries to the coil filaments.
Having found the optimal solution one can consider an ensemble of ions with deviations from the optimal starting parameters to determine the port geometry. In a last step the suggested ports can be fit into the CAD-program which takes all parts of the machine into account.

4.2 Results

W7-X consists of 5 identical modules each of 12 non-planar and 2 planar coils. The maximum distance between two coils is less the 0.7m. Figs. 7 and 8 show an overview over the complicated structure together with planned diagnostic ports. Fig. 8 indicates where access for the two ports (e.g.:

diagnostic: $D_{1,2,3}$; injection: $I_{1,2,3}$) could be possible.
A 2D-code can give good results for the poloidal but not toroidal deflection of ions. Preliminary studies with the CFN-code already in principle showed the possibility of HIBP on W7-X [32]. As the major result the minimum energy necessary to detect the plasma from the boundary to the centre was found to be 3MeV. But none of the planned ports can be used. Therefore the port geometry for HIBP has to be specified. These results were confirmed by the 3D calculations.
Three different injection scenarios were analysed by the 3D-orbit code and the corresponding port geometry were determined. In all cases the orbit behaviour is characterised by a self-focusing-effect. This means there is a small spread of secondary trajectories produced by one primary at the edge or near the centre. Therefore the detection of the electric potential over the full plasma seems to be possible. This self-focusing imposes high demands on the resolution of the analysing equipment.
Due to the best access to the plasma (see Fig. 8) the study started on the $\phi=0^{o}$-plane. Choosing the B-field into positive ϕ-direction the particle is deflected downward and therefore the upper port has to be the injection port. Taking into account the W7-X geometry, the according symmetric solution with opposite B-field direction can be chosen. The optimal central beam reaches the plasma centre (r_{min} <0.05m) as shown in Figs. 10a and 10b. The two ports are showing enough flexibility (Figs. 10 and 11). The main disadvantage of this solution is the conflict with already fixed diagnostics and heating systems (ECRH and NBI).
A second case was considered in the $\phi=22^{o}$- plane (compare Fig. 8). Choosing the opposite direction for B, the detection port is the upper one now. Due to the smaller coil distances the system is less flexible then the former. Additionally the injection and detection beam outside the cryostats are nearly in one plane and do not diverge (Figs. 12 and 13). Problems with place for the equipment is probable.
The third scenario is based on an injection in the $\phi=15^{o}$- plane and a detection port in the $\phi=22^{o}$- plane. The corresponding beams and ports as shown in Figs. 14-16 have better flexibility and access. Because of no problems with other devices this case is proposed for the HIBP at W7-X.
The parameters describing the geometry and location of the ports for the three cases are summarised in Table 2.

5. Future steps

The determination of the port geometry is an important step towards the planning of an HIBP for W7-X. Nevertheless detailed theoretical studies has to be done concerning the following problems:
1) B-field variation (β-dependence),
2) Design of the electrostatic deflection system,
3) Beam attenuation calculations and
4) Energy slowing down calculations.

1)The orbit calculations presented in this paper have been carried out for the standard vacuum magnetic B-field configuration. Because of planned W7-X operations up to β=5% corresponding cases have to be studied (e.g. β=2.5% and β=5%). For this the input data set has to be recalculated using appropriate MHD equilibrium codes (KW-code or the VMEC-code). Applying e.g. the VMEC-code the B-field components and the effective radius can be determined inside the last closed flux surface on the same 3D-grid points as chosen for the GOURDON-code. The distance from the coil filaments and the B-field outside the last closed flux surface can be taken from the β=0 % GOURDON-results. The variation of the trajectories with respect to β is expected to be small because of full optimisation of the W7-X stellerator (e.g. minimised Shafranov shift)

2) The probing beam trajectory in stellerators can be controlled completely by four sets of sweep plates. As a result, the beam can be easily adjusted to different magnetic configurations. The method of designing the electrostatic deflection system is described in [33] and was tested at CHS.

3) A detailed beam attenuation study has to be performed to determine the total signal current of doubly charged secondaries produced by electron and proton ionisation in the sample volume to decide which analysing method has to be chosen (current detection mode or particle counting method, Proca-Green type or multiple cell detector). From the 3D-orbit code the primary and secondary trajectories are known and therefore the attenuation can be calculated directly along the beam paths. The secondary current, coming from a sample volume (e.g. $r_k<r<r_{k+1}$), can be determined easily knowing the plasma densities and temperatures as well as the cross sections (see e.g. [4, 18, 23]):

$$I_k^{++} = I_0^{+}\ \lambda_{12}^{-1}\ \Delta r\ \exp\left(-\int_{R_1}^{r} \lambda_{12}^{-1} ds\right)\ \exp\left(-\int_{r}^{R_2} \lambda_{23}^{-1} ds\right)$$

where I_0 is the injection current, r is an ionisation point inside sample volume, $\Delta r = r_{k+1} - r_k$, R_1 and R_2 are the primary entry and secondary exit point, respectively and λ_{12} and λ_{23} the effective attenuation length of the primary and secondary, respectively.

4) Multiple Coulomb collisions in the plasma should result in a significant energy slowing down of the probing beam due to long path in the beam. This study can be done very similar to the intensity slowing down procedure as described above. The beam energy of a detected secondary which was ionised at a point r along the trajectory is given by:

$$W(r) = W_0 \exp\left(-\int_{R_1}^{r} \lambda_1^{-1} ds\right) \exp\left(-\int_{r}^{R_2} \lambda_2^{-1} ds\right)$$

where W_0 is the initial energy of the primary. Now the effective energy slowing down length of the primary and secondary (λ_1 and λ_2, respectively) has to be taken (see [18]) instead of the effective intensity attenuation lengths.

6. Conclusions

Using a 3D orbit code reference Cs-ion trajectories were calculated to determine the optimal port geometry for an HIBP system on W7-X for the standard B_0=2.5T case. The minimum energy necessary to determine the electrostatic potential even in the plasma centre was found to be 3MeV, which correspond to present HIBP technique (TEXT/UG 2MeV Tl). This is possible due to a self-focusing effect of secondaries, which on the other hand requires high resolution of the analysing system. The ports are large enough to ensure good flexibility with respect to smaller changes in the future design of W7-X. The best solution not being in conflict with other diagnostics or heating systems was found to be injection in the ϕ=15°-plane and detection in the ϕ=22°-plane.

Acknowledgement

The author would like to thank A. Malaquias for many useful discussions , J. Kiesslinger in support of the GOURDON-code calculations, F. Kerl and R. Holzthüm for preparing the CAD-plots of the HIBP-ports.

References

/1/ Hickok R.L., IEEE Trans. Plasma Phys., 22 (4) 287, 1994 and Ref. therein.
/2/ Crowley T.P., IEEE Trans. Plasma Phys., 22 (4) 291, 1994.
/3/ Dnestrovskij Yu.N., et. al., IEEE Trans. Plasma Phys., 22 (4) 310, 1994.
/4/ Cabral J.A.C., et. al., IEEE Trans. Plasma Phys., 22 (4) 351, 1994.
/5/ Forster J.C., et. al., IEEE Trans. Plasma Phys., 22 (4) 359, 1994.
/6/ Melnikov A.V., et. al., IEEE Trans. Plasma Phys., 22 (4) 363, 1994.
/7/ Aceto S.C., Connor K.A., Schwelberger, J.G., IEEE Trans. Plasma Phys., 22 (4)389, 1994.
/8/ Schwelberger J.G., Report DOE/ER/542-41-135/FRCR-450, 1994.
/9/ Hamada Y., et. al., Report NIFS-273, 1994.
/10/ Schwelberger J.G., et. al., Rev. Sci. Instrum., 63 (10) 4571, 1992.
/11/ Schoch P.M., et. al., Rev. Sci. Instrum, 59 (8) 1646, 1988.
/12/ Aceto S.C., et. al., Rev. Sci. Instrum., 63 (10) 4568, 1992.
/13/ Bondarenko, I.S., et. al., 22 EPS Bournemouth, 1995.
/14/ Bugarya V.I., et. al., Nuclear Fusion, 25 (12) 1707, 1985.
/15/ Fujisawa A., et. al., Report DOE/ER/542-41-147/FRCR-466, 1995.
/16/ Maßberg, H., et. al., Phys. Fluids B5, 3627, 1993.
/17/ Itoh K., et. al., IEEE Trans. Plasma Phys., 22 (4) 376, 1994 and Ref. therein.
/18/ Fujisawa A., et. al., IEEE Trans. Plasma Phys., 22 (4) 395 1994.
/19/ Fujisawa A., et. al., Report NIFS-272, 1994.
/20/ Taniike A., et.al., IEEE Trans. Plasma Phys., 22 (4) 430, 1994.
/21/ Ishii K., IEEE Trans. Plasma Phys., 22 (4) 332, 1994.
/22/ Saravia E., Castracane J., Woo J.T., Rev. Sci. Instrum., 61 (10) 2987, 1990.
/23/ Schwelberger J.G., Connor K.A., IEEE Trans. Plasma Phys., 22 (4) 418, 1994.
/24/ Green P.S., Proca G.A., Rev. Sci. Instrum., 41 (12) 1778, 1970.
/25/ Keating L.M., et. al., IEEE Trans. Plasma Phys., 22 (4) 424, 1994.
/26/ Hamada Y., et. al., Rev. Sci. Instrum., 63 (10) 4446, 1992
/27/ Leisenfelder H.J., et. al., Rev. Sci. Instrum., 63 (10) 4579, 1992.
/28/ Fujisawa.A., et. al., Report NIFS-317, 1994.
/29/ Cabral J.A.C., et. al., Report CFN 5/94, 1994.
/30/ Varandas C.A.F., et. al., Fusion Technology, 1532, 1992.
/31/ private communication with A. Malaquias, 1995.
/32/ Malaquis A., Teubel, A., internal report on orbit calculations, Lisbon 1995.
/33/ Fujisawa.A., et. al., Rev. Sci. Instrum., 63 (7) 3694, 1992.

Figure Captions

Fig.1. Projection of particle trajectories onto a plane for the 500keV TEXT HIBP. The 3 secondary trajectories shown correspond to 3 entrance slits in the detector (from [2]).

Fig. 2. Detection grid for caesium ions with the ISX-B HIBP at Bt=12.3 kG. The grid describes the beam energy (expressed in terms of the accelerator voltage in kV) and the initial injection angle (in degrees) needed to reach the intersection points in the plasma. Note that this figure does not include any particle trajectories (from [2]).

Fig. 3. Dependence of gold beam attenuation on the central electron temperature. The electron temperature and density profiles are assumed to be parabolic and flat, respectively. (a) 5.6MeV beam for the 3T standard operation. (b) 1.4MeV beam for the half magnetic field operation (from [18]).

Fig. 4. Dependence of beam energy attenuation on the central plasma temperature. The electron and proton have the same temperature and the temperature and density profiles are assumed to be parabolic and flat, respectively. (a) 5.6MeV beam for the 3T standard operation (b) 1.4MeV beam for the half magnetic field operation (from [18]).

Fig. 5. (a) Schematic view of the 500keV HIBP on TEXT (from [2]).
(b) Schematic view of the 6MeV HIBP on LHD (from [18]).

Fig. 6. (a) Schematic drawing of a Proca-Green parallel plate energy analyser (from [2]).
(b) Energy analyser detector split plates. Front view of the 4 plates as seen by the beam (from [2]).

Fig. 7. Top view of coils and ports of W7-7X.

Fig. 8. ϕ - θ plot of coils, ports and structure elements of a W7-X module. The location of the injection and detection ports for the three cases are indicated by I_i and D_i , (i=1, 2, 3), respectively.

Fig. 9. Sketch of the geometry in the R-z plane and x - y plane. Fixed parameters are given.

Fig. 10. Reference beam with starting position parameters given in the plot, for the 0^0-case. Two secondaries are shown born at the edge and in the centre of the plasma. (a) R-z plot includes additionally the coil and port locations as well as the flux surface with r_{eff}=0.1m. (b) Top view (notice the scales of x and y axis are different).

Fig. 11. CAD plots of the injection (blue) and detection (read) ports for the 0^0-case including the full coil geometry.

Fig. 12. Reference beam with starting position parameters given in the plot, for the 22^0-case. Two secondaries are shown born at the edge and in the centre of the plasma. (a) R-z plot includes additionally the cryostat and the flux surfaces with r_{eff}=0.1m r_{eff}=a, respectively. (b) Top view.

Fig. 13. CAD plots of the injection (blue) and detection (read) ports for the 22^0-case including the full coil geometry.

Fig. 14. Reference beam with starting position parameters given in the plot, for the $15^0/22^0$-case. Two secondaries are shown born at the edge and in the centre of the plasma. (a) R-z plot includes additionally the cryostat and the flux surfaces with r_{eff}=0.1m r_{eff}=a, respectively. (b) Top view.

Fig. 15. The same as Fig. 14. but with additional beams varying in their initial parameters from the reference beam:
$\theta_0=12^0\text{-}20^0$, $\theta_{v0}=(85.5^0 - 86.5^0) - \theta_0$, $\phi_{v0}=6.0^0 - 7.0^0$.

Fig. 16. CAD plots of the injection (blue) and detection (read) ports for the $15^0/22^0$-case including the full coil geometry.

Fig. 17. Top view of W7-X with possible locations in different modules of the injection (blue) and detection (read) ports for the $15^0/22^0$-case.

	Device	Institut	Country	HIBP parameter		Machine-parameter						
				W [keV]	Species	R [cm]	a [cm]	B_t [T]	I_p [kA]	n_e [E13/ccm]	T_e(0) eV	T_i(0) eV
Stellerators												
	ATF	ORNL	USA	700	Cs+ Tl+	210	27	0.5 - 1		0.5 - 10	500 - 1000	200
	CHS	NIFS	Japan	100	Cs+	95	20 - 30	0.4 - 2.4		1 - 3	300	150
	Heliotron-E	Uni Kyoto	Japan	90	Cs0	220	20	2		0.5 - 3.5	250 - 1000	200
	LHD	NIFS	Japan	6000	Au+ Tl+	375	60	3		0.1 - 10	10000	10000
	TJ-II Spain	CIEMAT	Spain	200	Cs+	150	10 - 20	1		2 - 10	500 - 1000	200 - 400
	W7-X	IPP	Germay	2000	Tl+	550	50	2,5		1 - 20		
Tokamaks												
	ISTTOK	IST	Portugal	400	Cs+	46	8.5	0.4 - 0.6	6 - 12	0.5 - 1.5	100 - 300	200 - 400
	ISX-B	ORNL	USA	160	Cs+ Tl+	93	26	1.2	160	4	500 - 700	300
	JIPPT-II-U	NIFS	Japan	500	Tl+	95	24	3	200	6 - 12	800	600
	RENTOR	Rensselaer PI	USA	30	Cs+	45	12	0.4	10 - 25	0.2	100	25
	ST	Princeton Uni	USA	100	Tl+	109	12	1.4	10 - 21	1.6	300	150
	T-10	Kurchatov Inst.	Russia	220			30	1.5 - 3	135 - 200			
	TEXT	Rensselaer PI	USA	500	Cs+ Tl+	100	26	2.2	200	1.2 - 5	1000	600
	TEXT-UG	Rensselaer PI	USA	2000	Tl+	100	26	2.2	200	1.2 - 5	1000	600
	TJ-I	CIEMAT	Spain	100	Cs+	30	9	1.4	20 - 40	2 - 3	300	100
	TM-4	Kurchatov Inst.	Russia	120	Cs+	54	8.5	1.3 - 2	21 - 26	0.6 - 4.5	600	120

Table 1.

			1st case 0/0	2nd case 22/22	3rd case 15/22
	B-direction	wrt. to phi-direction	positive	neagative	negative
injection port					
	outer central point	(x1, y1, z1) [m]	(8.000 ,-0.100 , 1.514)	(7.673 , 3.657 , 2.080)	(8.257 , 2.017 , 0.795)
	inner central poin	(x2, y2, z2) [m]	(6.000 ,-0.100 , 1.514)	(5.181 , 1.847 ,-0.160)	(5.267 , 1.582 ,-0.115)
	hight	h [m]	0.420	0.400	0.4
	width	w [m]	0.200	0.250	0.3
	rotation angle around				
	central axis	theta [degree]	0	-20	0
detection port					
	outer central point	(x1 , y1 , z1) [m]	(8.000 ,-0.043 , 0.543)	(7.445 , 4.101 , 5.660)	(7.167 , 4.570 , 2.820)
	inner central poin	(x2 , y2 , z2) [m]	(6.000 , 0.114 , 0.543)	(5.118 , 2.015 , 1.510)	(5.157 , 1.912 , 1.020)
	hight	h [m]	0.714	0.7	0.7
	width	w [m]	0.330	0.35	0.4
	rotation angle around				
	central axis	theta [degree]	0	-20	-25

Table 2.

Fig. 1.

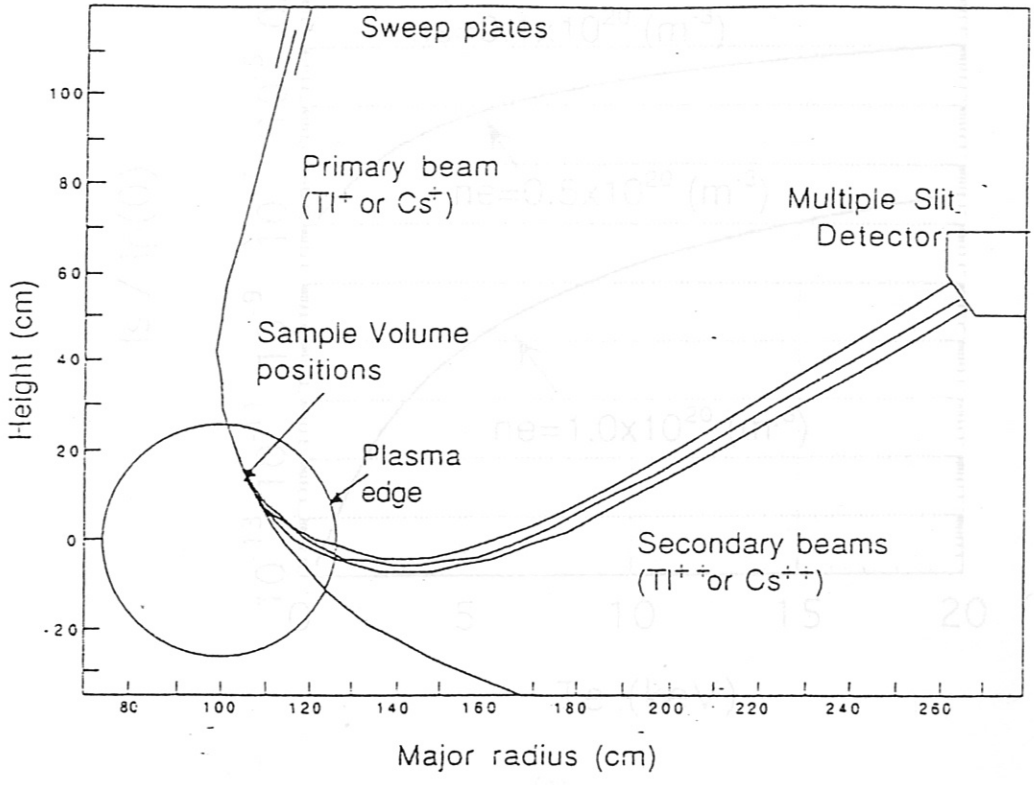
Sweep plates
Primary beam
(Tl+ or Cs+)
Multiple Slit
Detector
Sample Volume
positions
Plasma
edge
Secondary beams
(Tl++ or Cs++)
Height (cm)
Major radius (cm)
100
80
60
40
20
0
-20
80
100
120
140
160
180
200
220
240
260

Fig. 2.

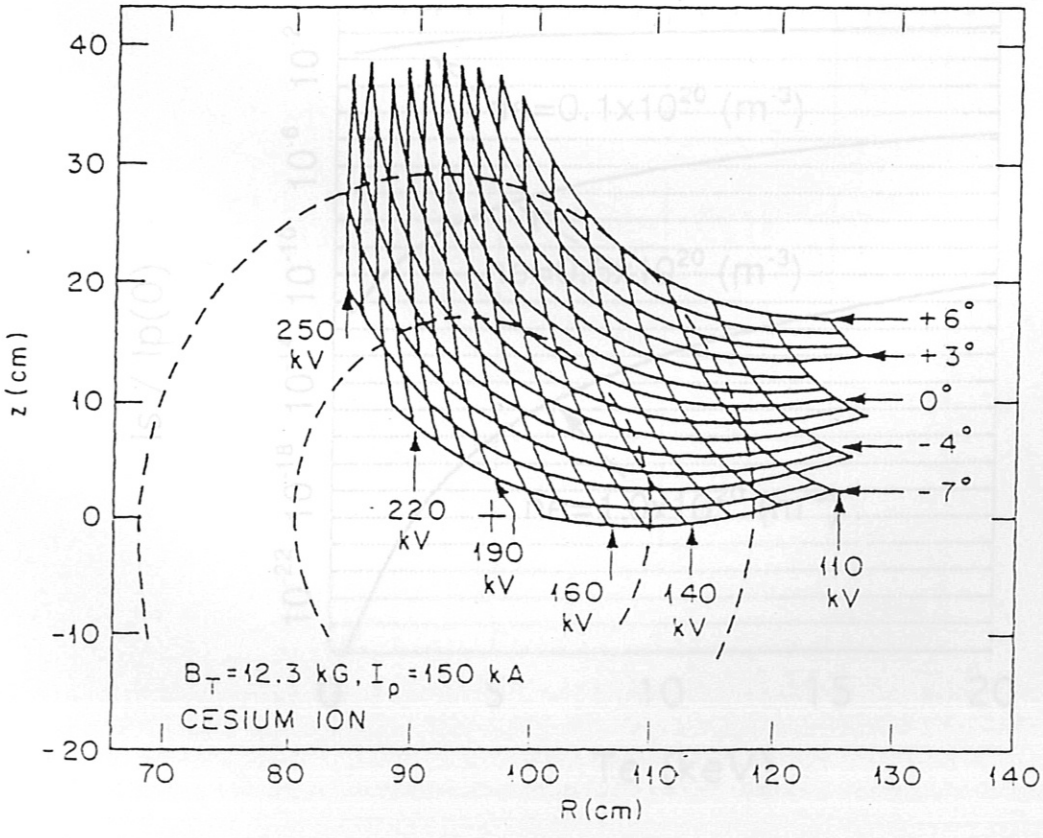
250
kV
220
kV
190
kV
160
kV
140
kV
110
kV
+6°
+3°
0°
-4°
-7°
B_T=12.3 kG, I_p=150 kA
CESIUM ION
z (cm)
R (cm)
40
30
20
10
0
-10
-20
70
80
90
100
110
120
130
140

Fig. 3.

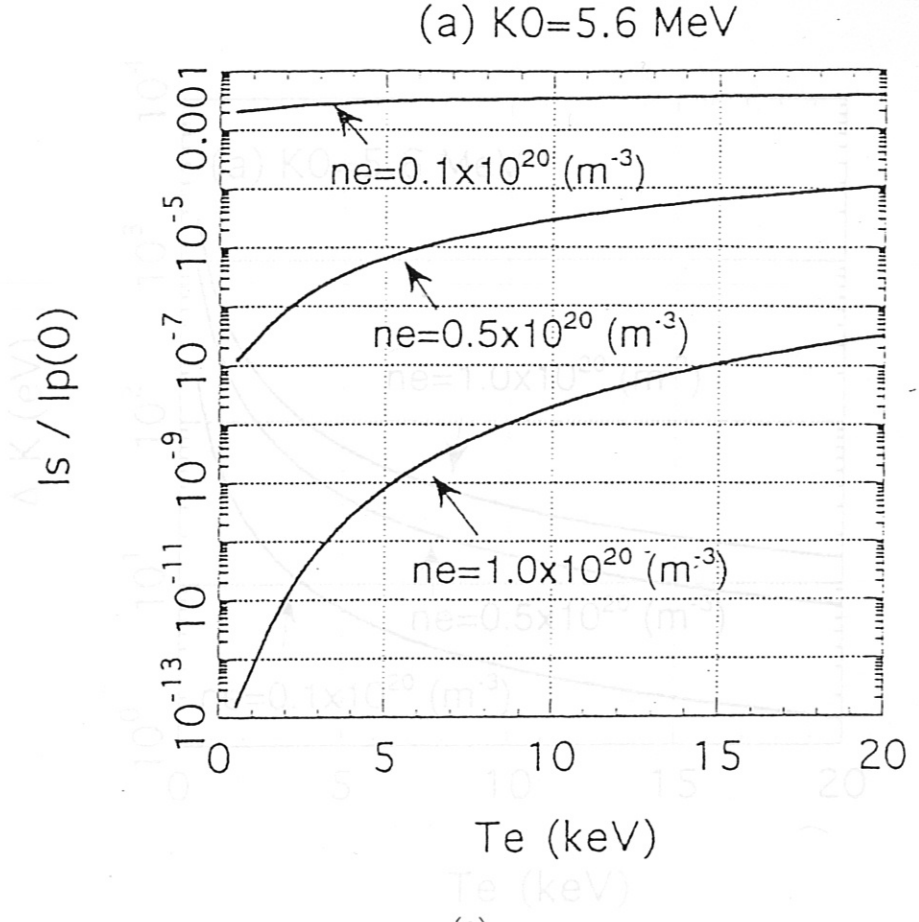
(a) K0=5.6 MeV
Is / Ip(0)
0.001
10^{-5}
10^{-7}
10^{-9}
10^{-11}
10^{-13}
ne=0.1x10^{20} (m^{-3})
ne=0.5x10^{20} (m^{-3})
ne=1.0x10^{20} (m^{-3})
0
5
10
15
20
Te (keV)

(a)

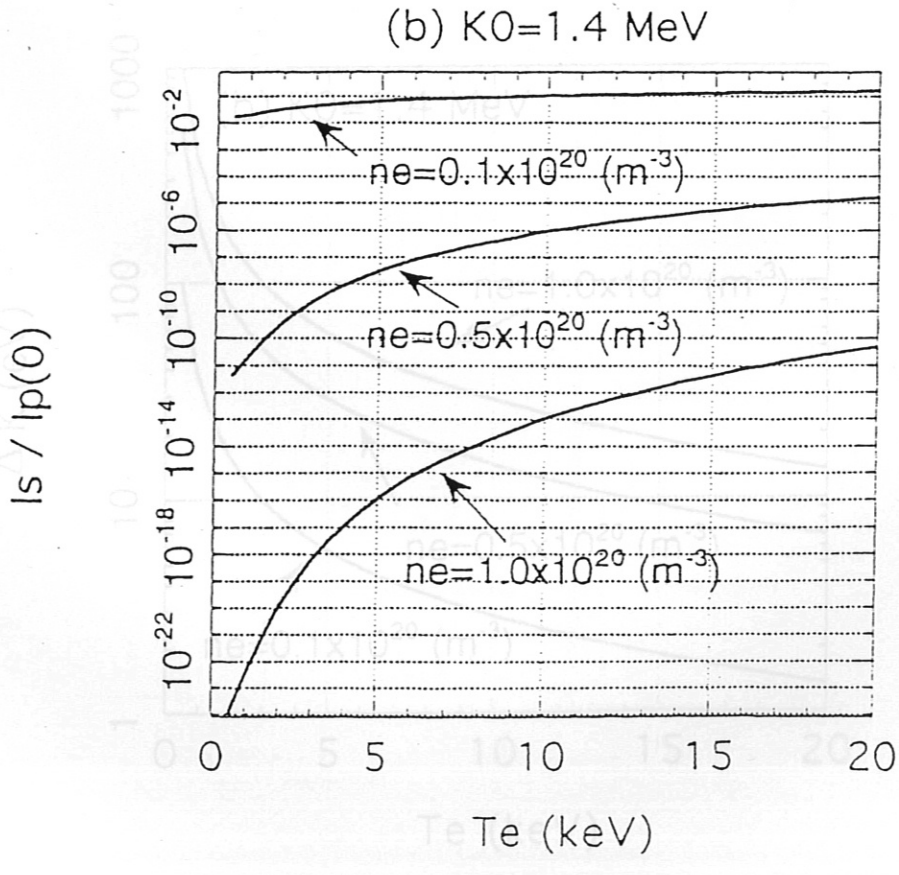
(b) K0=1.4 MeV
Is / Ip(0)
10^{-2}
10^{-6}
10^{-10}
10^{-14}
10^{-18}
10^{-22}
ne=0.1x10^{20} (m^{-3})
ne=0.5x10^{20} (m^{-3})
ne=1.0x10^{20} (m^{-3})
0
5
10
15
20
Te (keV)

Fig. 4.

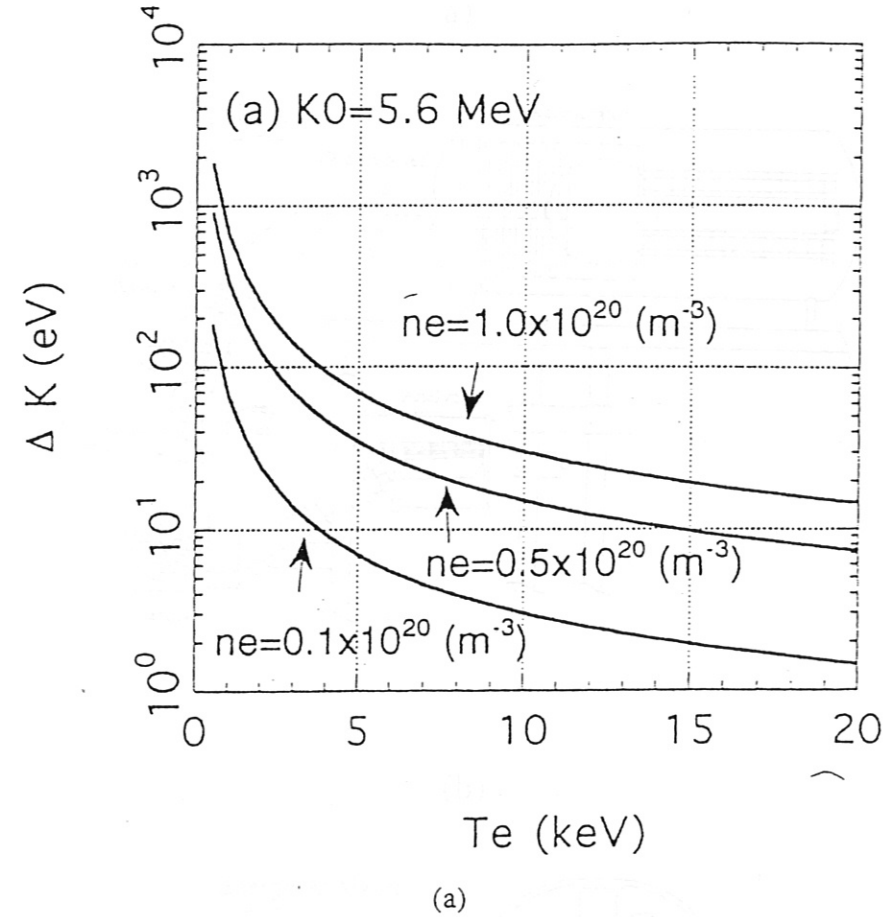
(a) K0=5.6 MeV
ne=1.0x10^20 (m^-3)
ne=0.5x10^20 (m^-3)
ne=0.1x10^20 (m^-3)
Δ K (eV)
Te (keV)
10^0
10^1
10^2
10^3
10^4
0
5
10
15
20

(a)

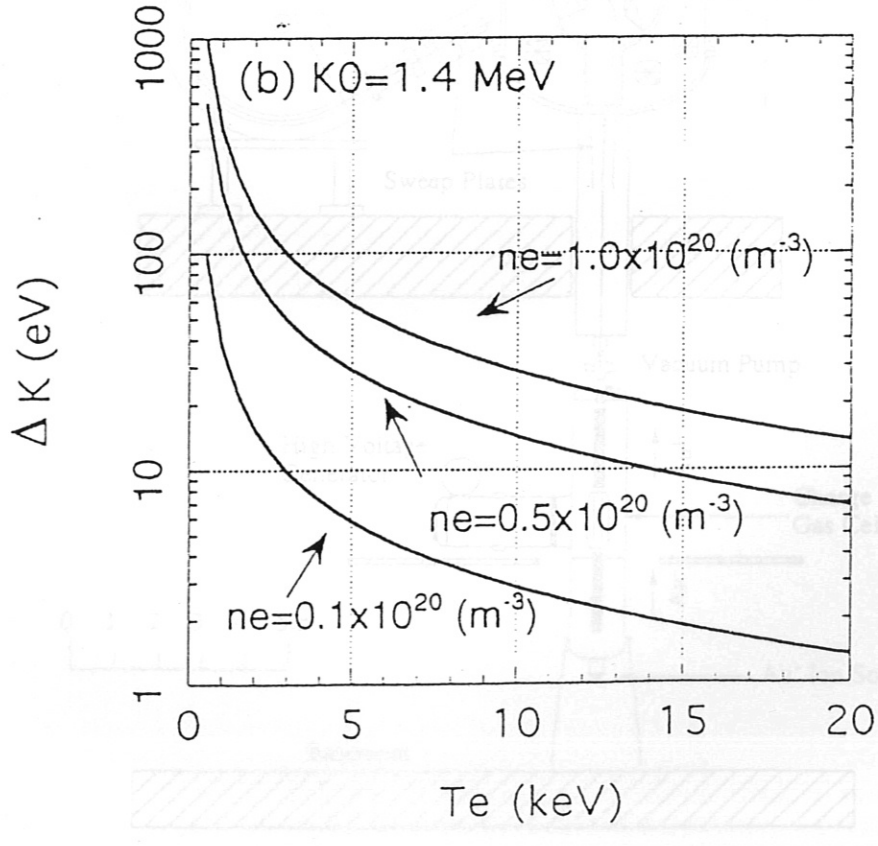
(b) K0=1.4 MeV
ne=1.0x10^20 (m^-3)
ne=0.5x10^20 (m^-3)
ne=0.1x10^20 (m^-3)
Δ K (eV)
Te (keV)
1
10
100
1000
0
5
10
15
20

Fig. 5.

(a)

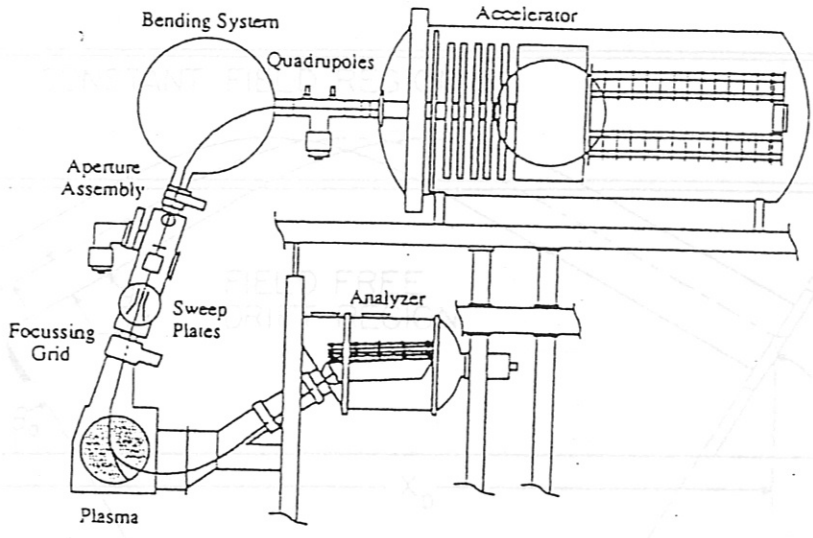
Bending System
Quadrupoles
Accelerator
Aperture Assembly
Sweep Plates
Focussing Grid
Analyzer
Plasma

(b)

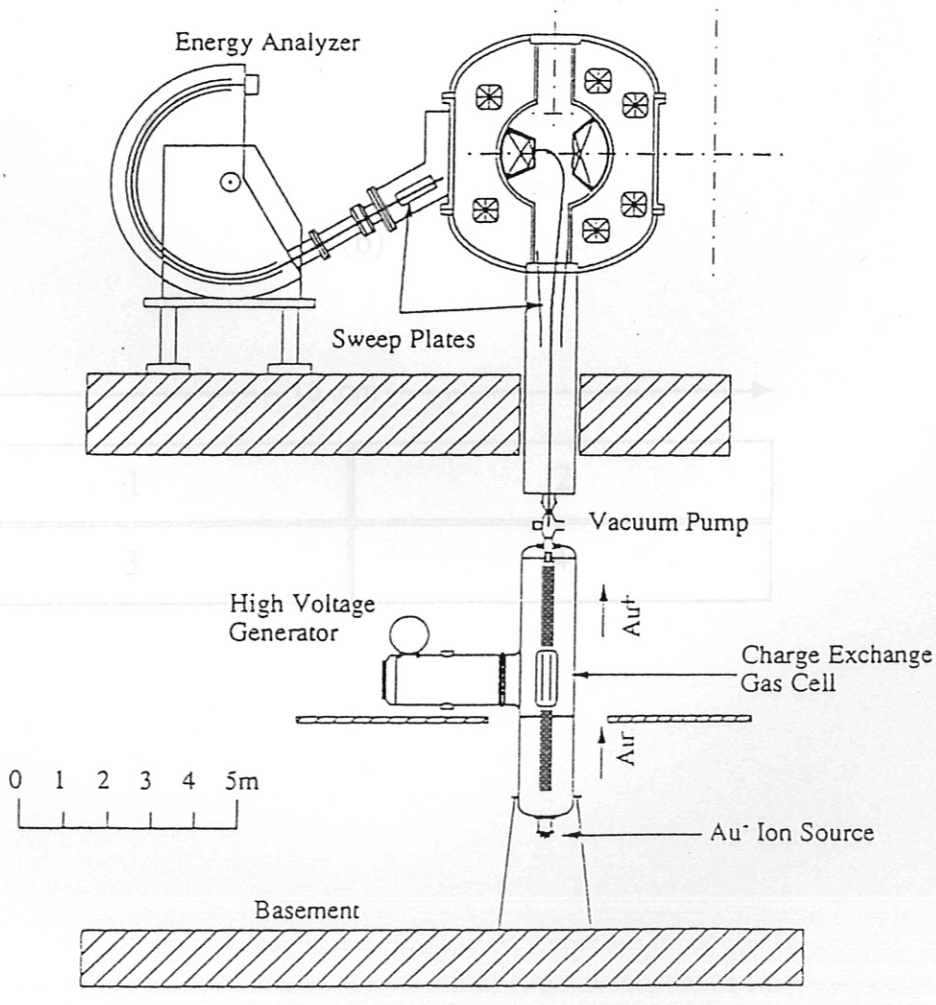
Energy Analyzer
Sweep Plates
Vacuum Pump
High Voltage Generator
Au+
Charge Exchange Gas Cell
Ar
0 1 2 3 4 5m
Au⁻ Ion Source
Basement

Fig. 6.

(a)

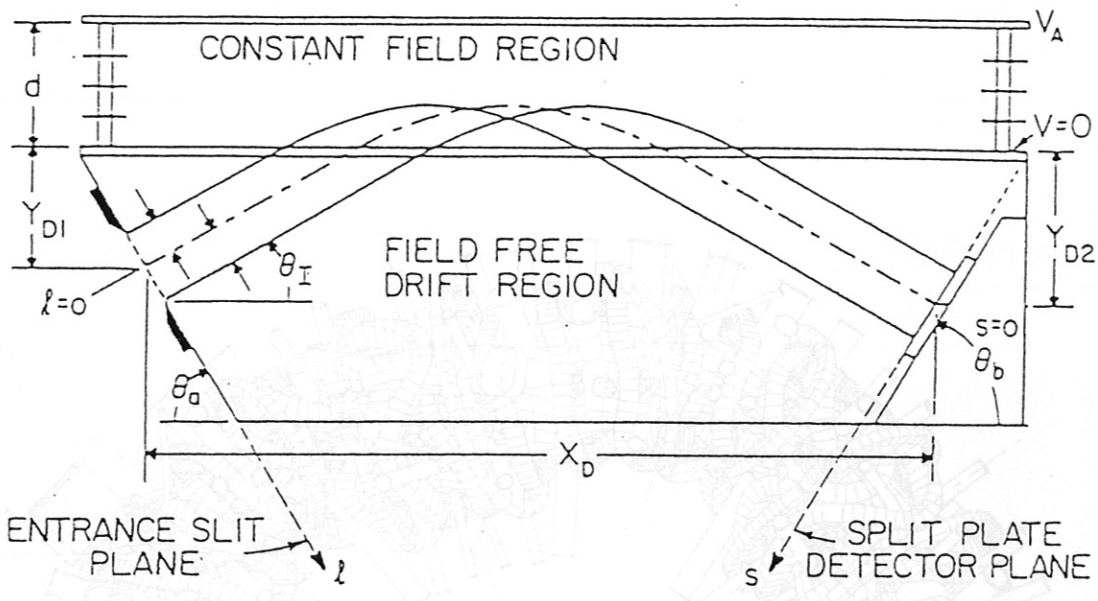
CONSTANT FIELD REGION
V_A
d
V=0
Y_{D1}
Y_{D2}
FIELD FREE
DRIFT REGION
θ_I
ℓ=0
s=0
θ_b
θ_a
X_D
ENTRANCE SLIT
PLANE
ℓ
SPLIT PLATE
DETECTOR PLANE
s

(b)

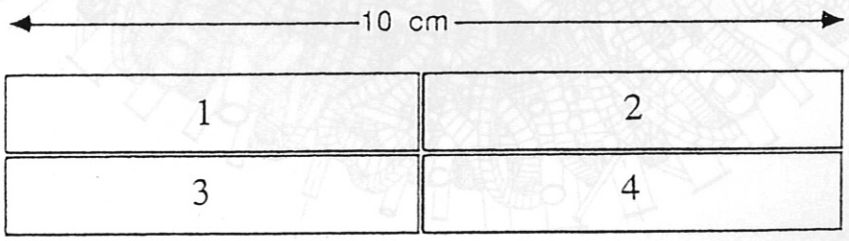
10 cm
1
2
3
4

Fig. 7

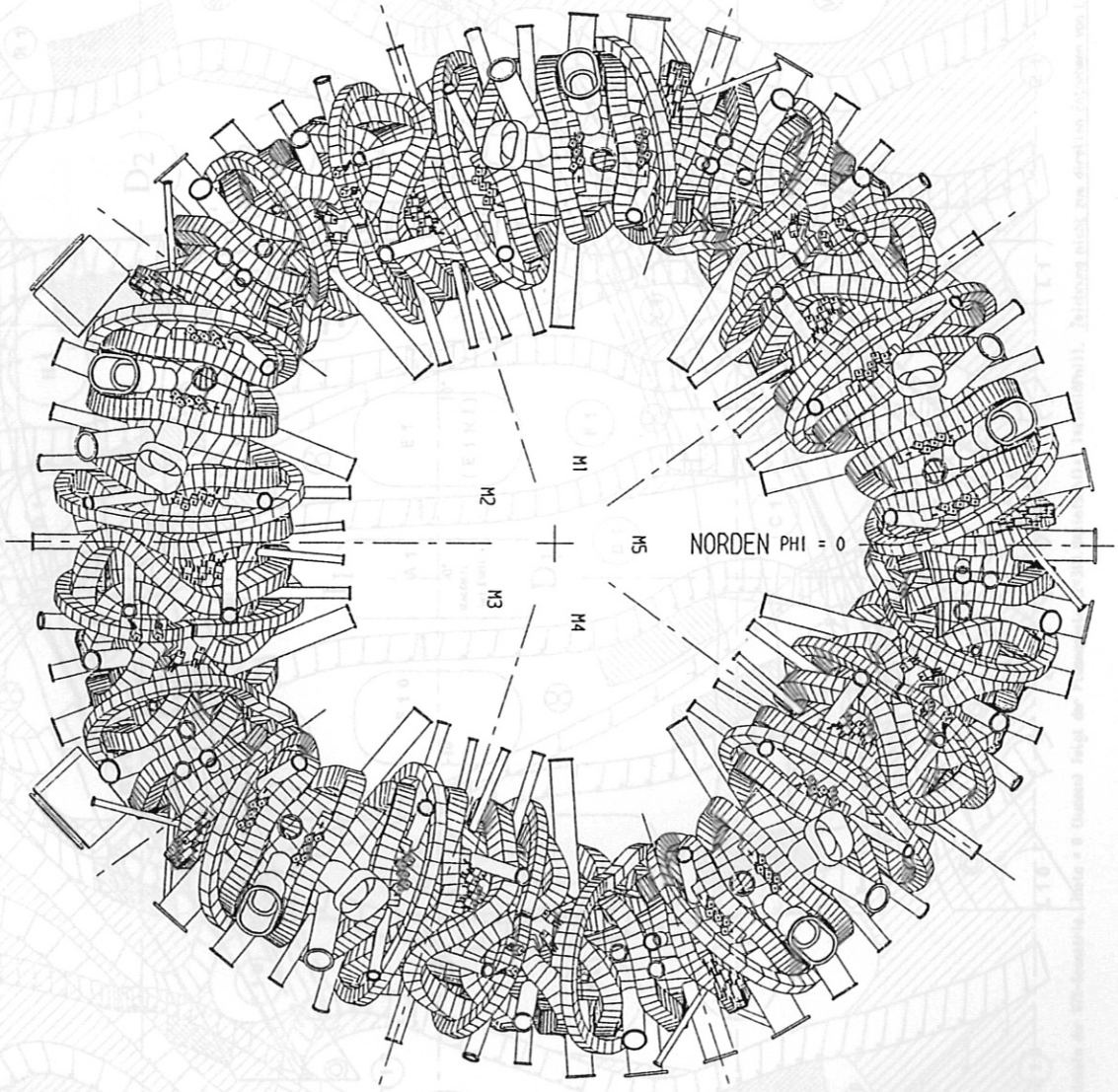

Fig. 8

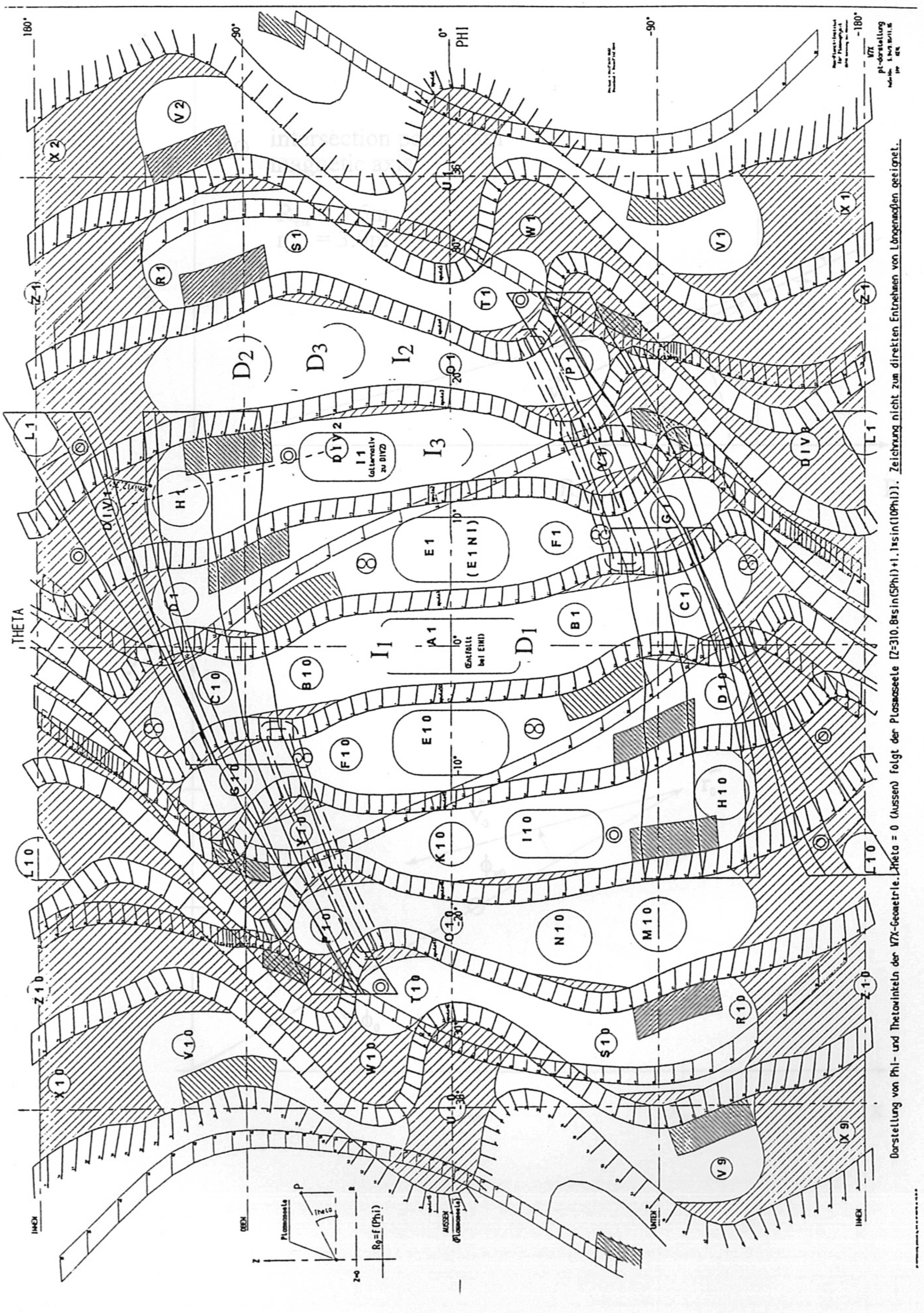
Darstellung von Phi- und Thetawinkeln der W7X-Geometrie. Theta = 0 (Aussen) folgt der Plasmaseele [Z=310.8*sin(5Phi)+1.1*sin(10Phi)]. Zeichnung nicht zum direkten Entnehmen von Längenmaßen geeignet.

Fig. 9.

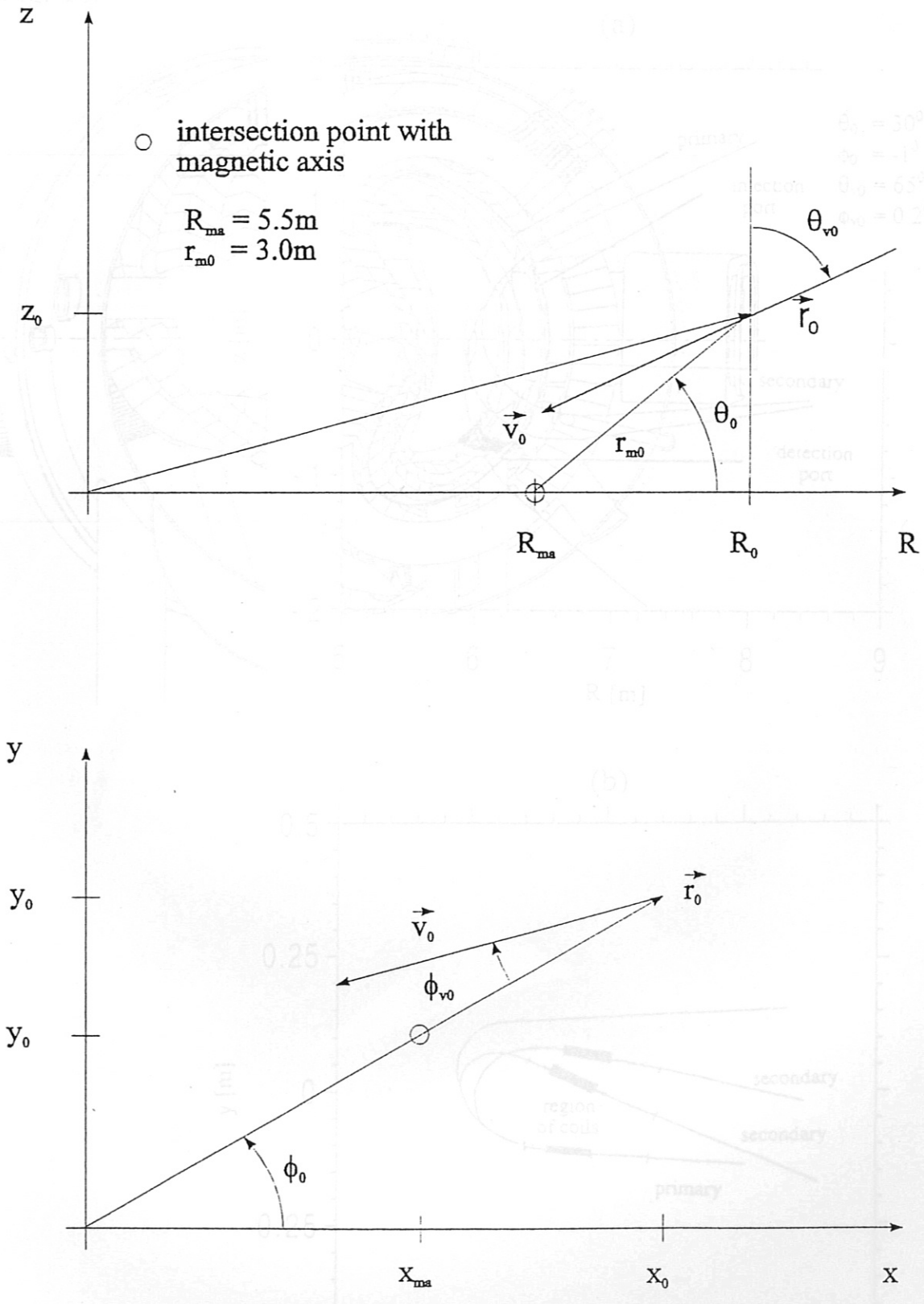
z
intersection point with magnetic axis
R_{ma} = 5.5m
r_{m0} = 3.0m
z_0
θ_{v0}
$\vec{r}_0$
$\vec{v}_0$
r_{m0}
θ_0
R_{ma}
R_0
R
y
y_0
y_0
$\vec{r}_0$
$\vec{v}_0$
ϕ_{v0}
ϕ_0
x_{ma}
x_0
x

Fig. 10.

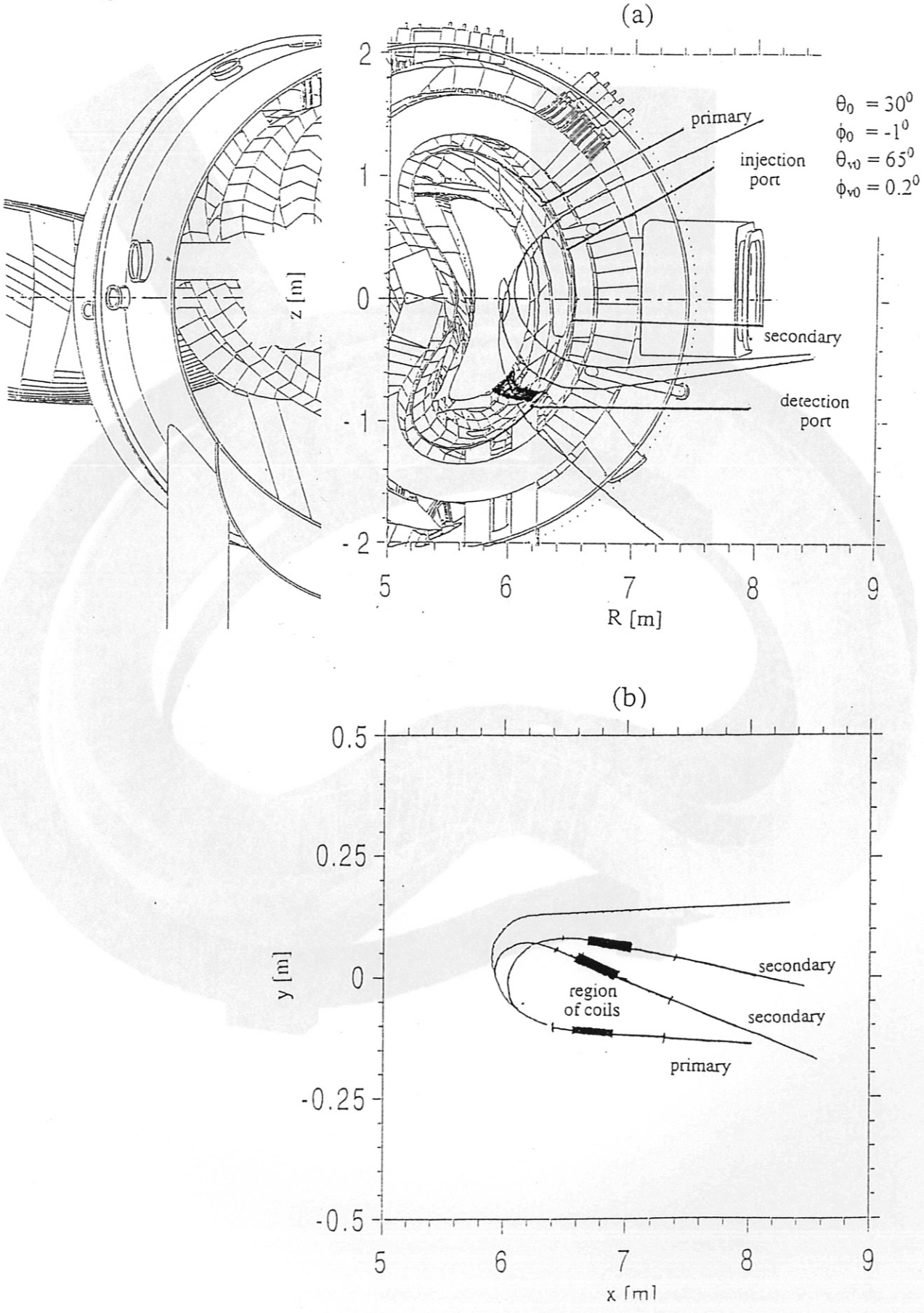
(a)
primary
injection port
secondary
detection port
$\theta_0 = 30^0$
$\phi_0 = -1^0$
$\theta_{v0} = 65^0$
$\phi_{v0} = 0.2^0$
z [m]
R [m]
(b)
region of coils
secondary
secondary
primary
y [m]
x [m]

Fig. 11a.

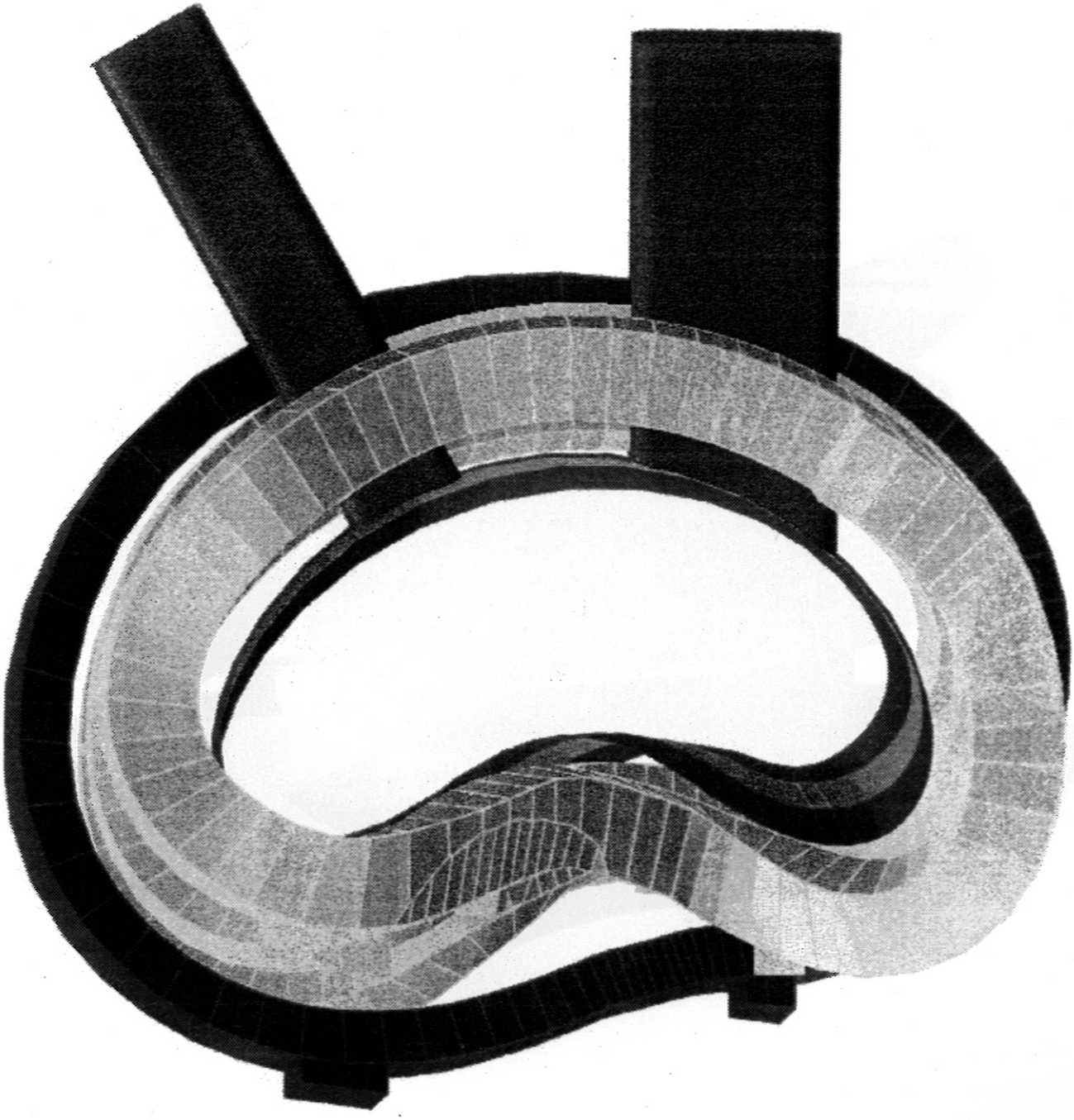

Fig. 11b.

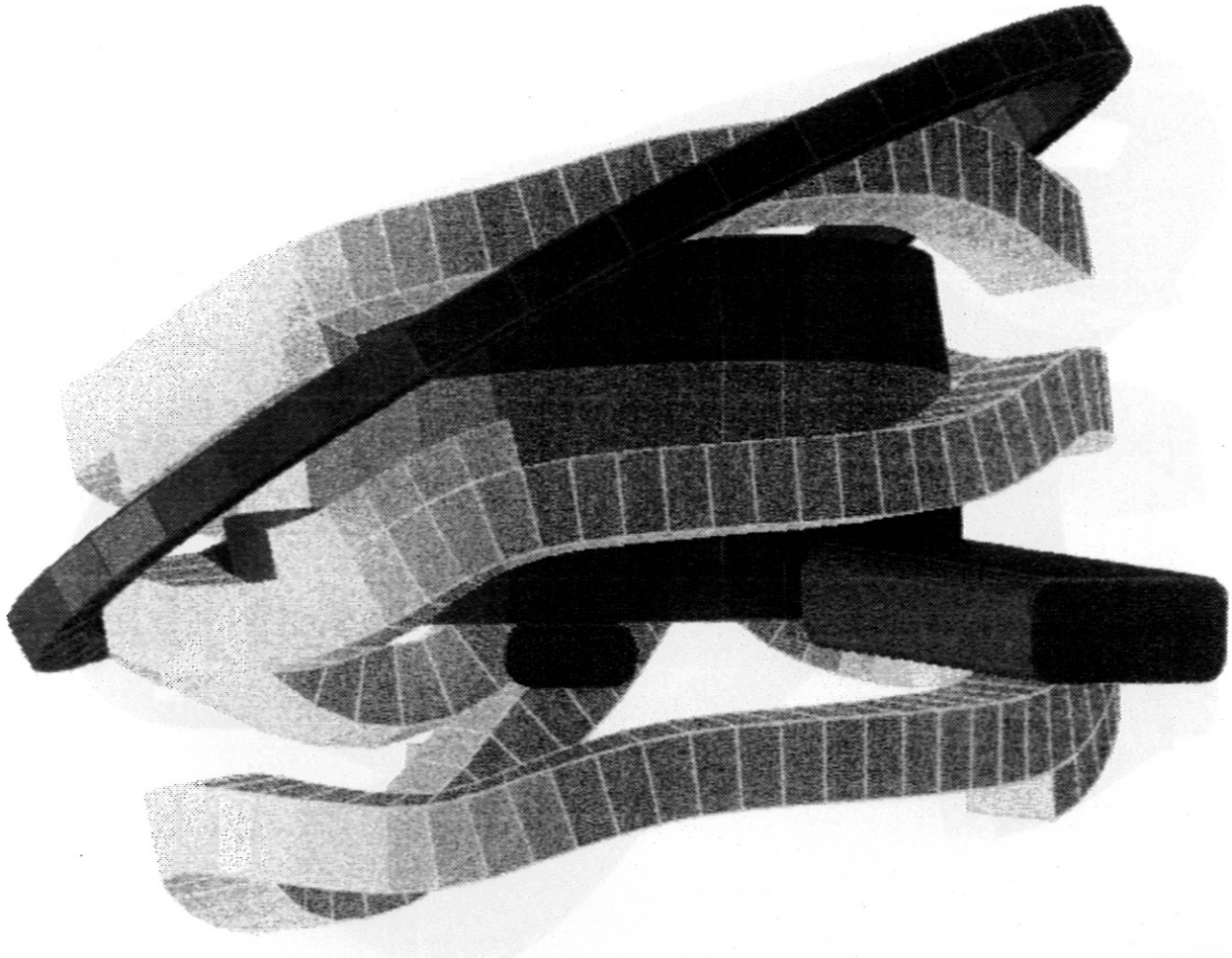

Fig. 11c

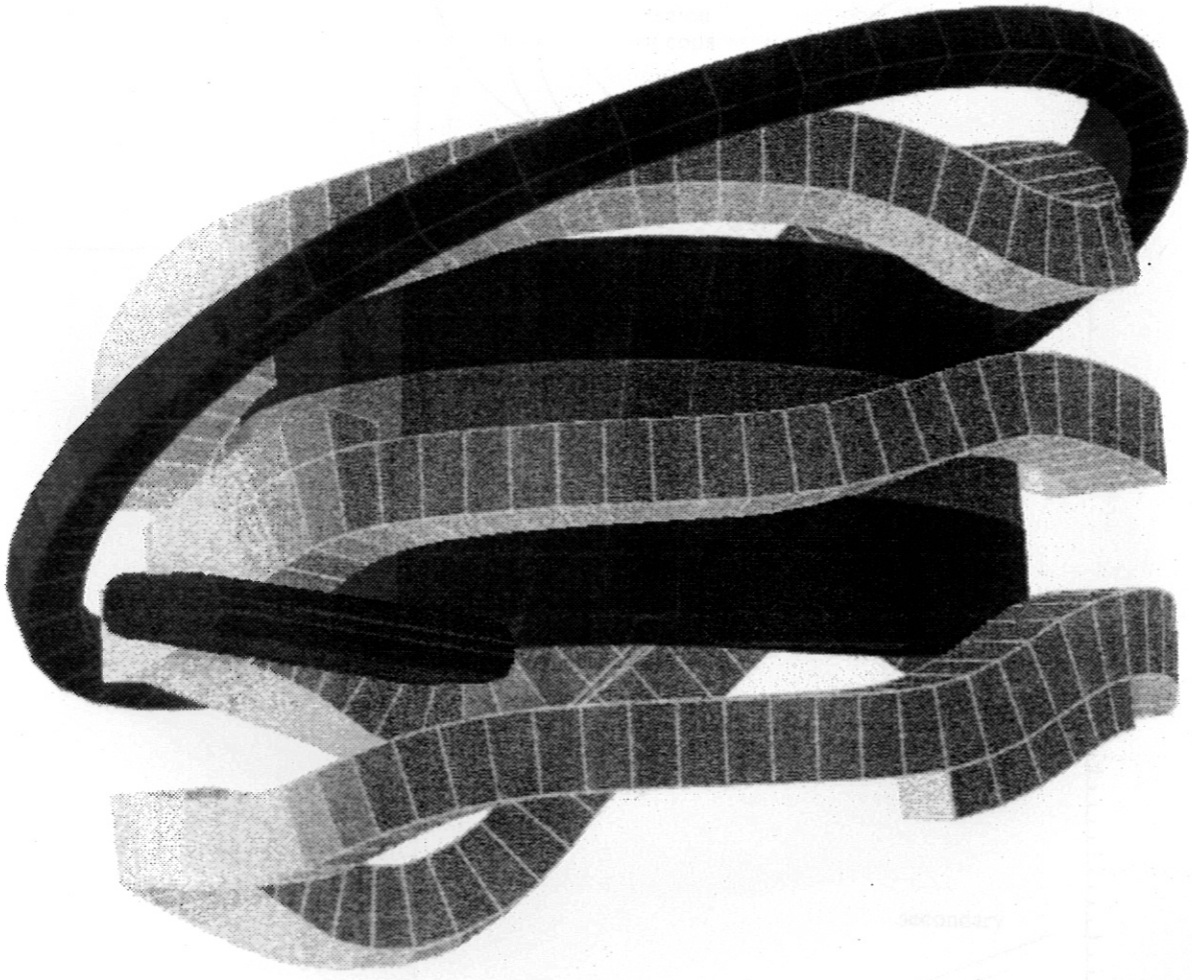

Fig. 12.

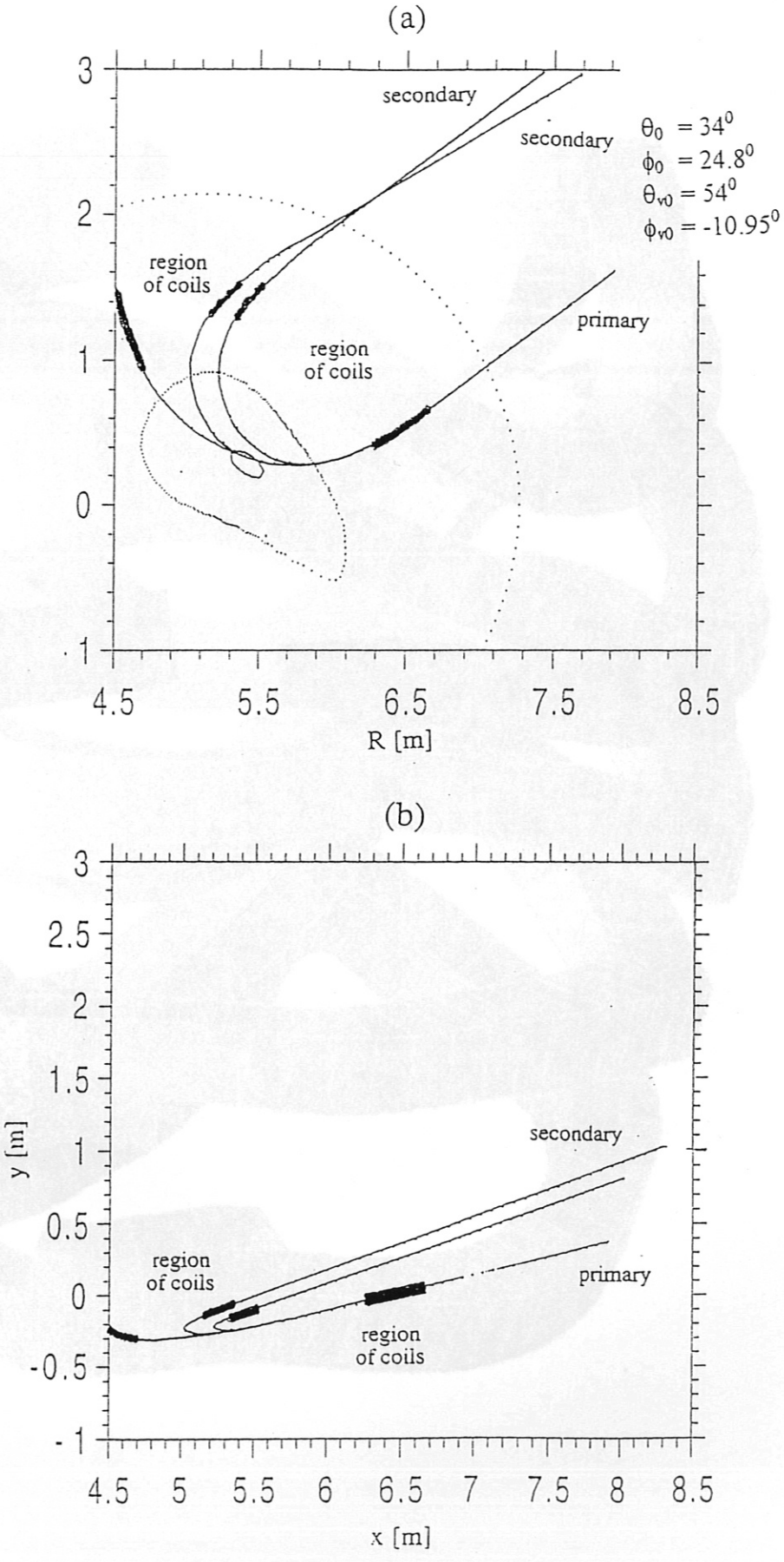
(a)
secondary
secondary
$\theta_0 = 34^0$
$\phi_0 = 24.8^0$
$\theta_{v0} = 54^0$
$\phi_{v0} = -10.95^0$
region of coils
region of coils
primary
3
2
1
0
-1
4.5
5.5
6.5
7.5
8.5
R [m]
(b)
3
2.5
2
1.5
1
0.5
0
-0.5
-1
y [m]
secondary
region of coils
primary
region of coils
4.5
5
5.5
6
6.5
7
7.5
8
8.5
x [m]

Fig. 13a.

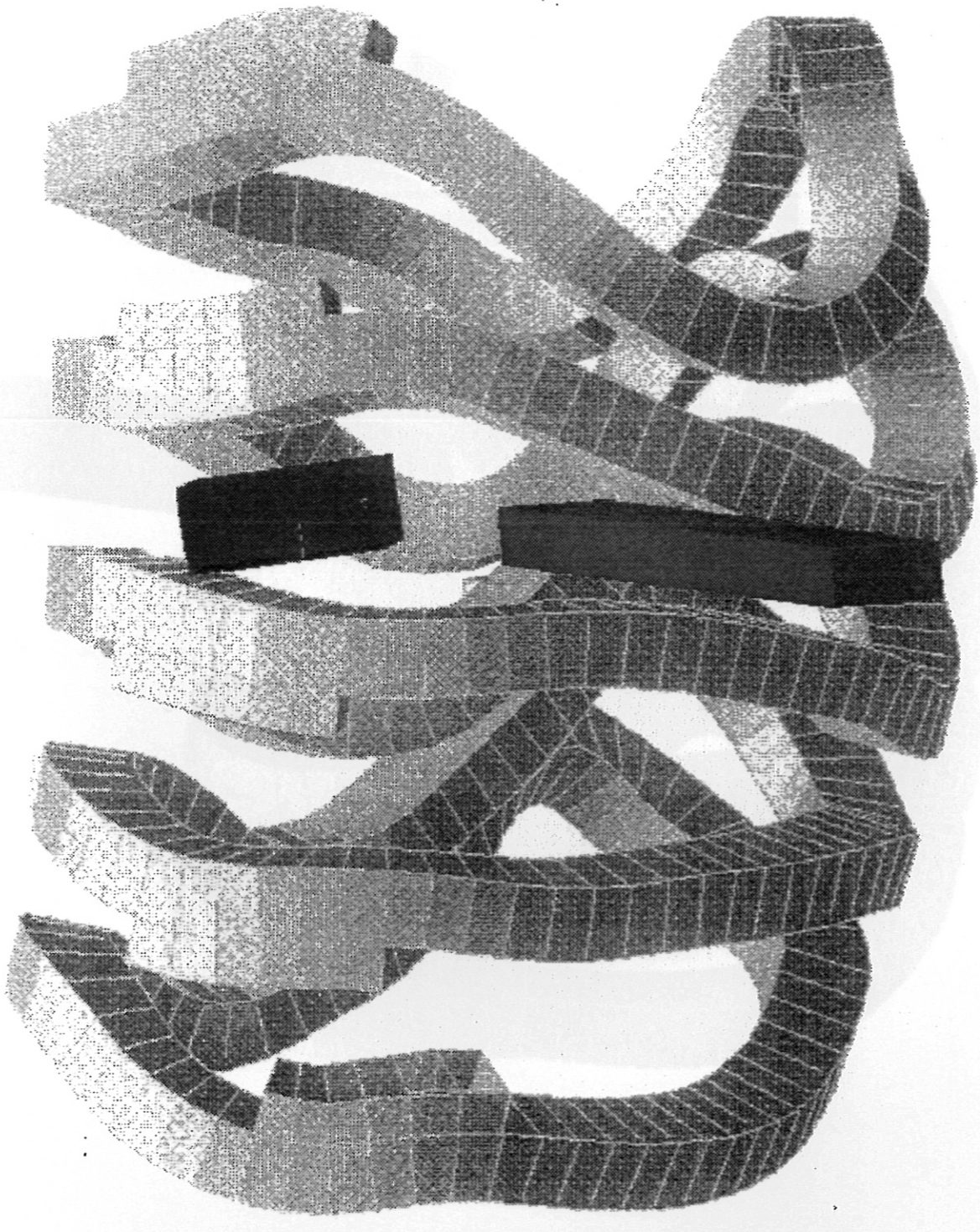

Fig. 13b.

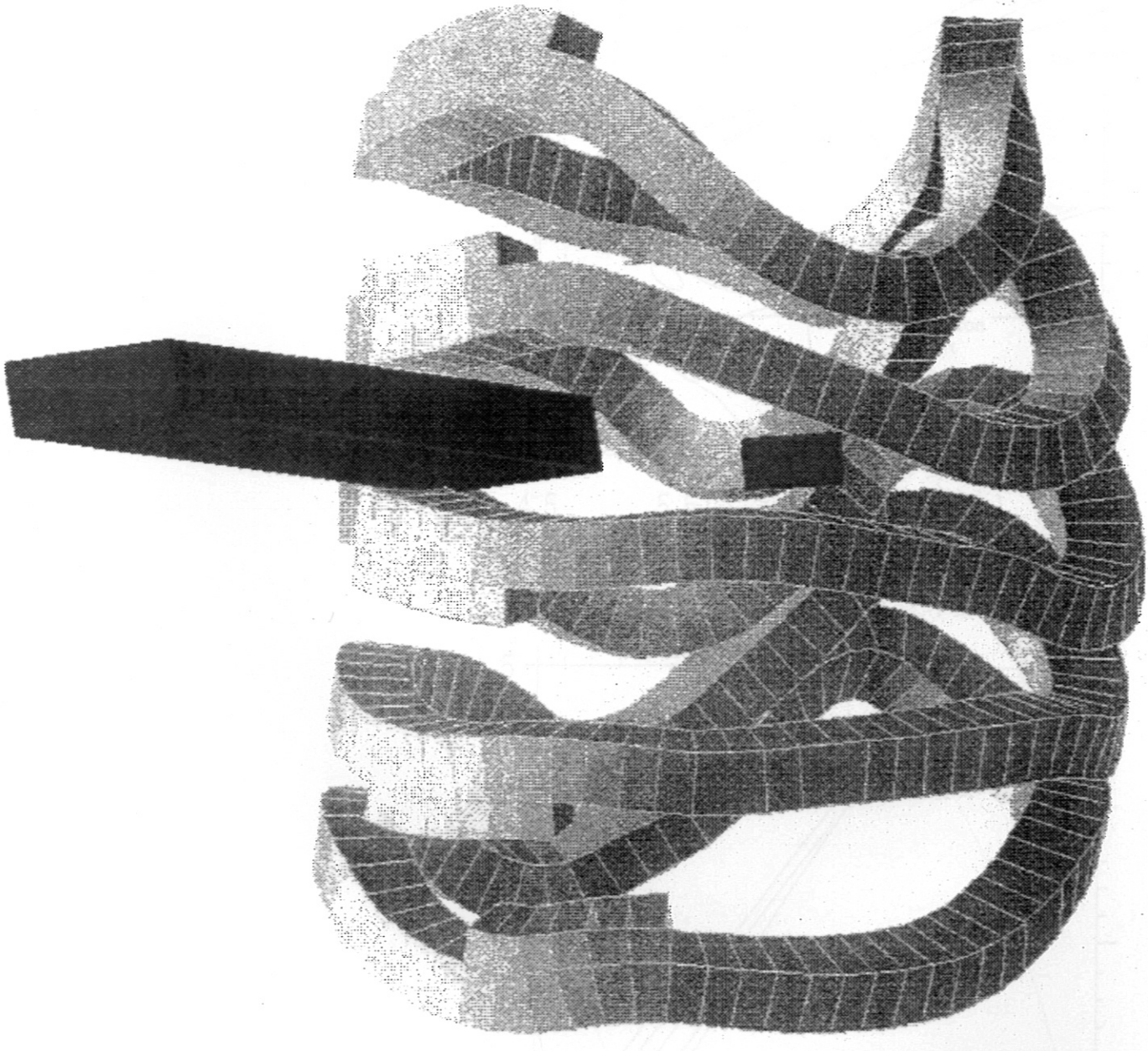

Fig. 14.

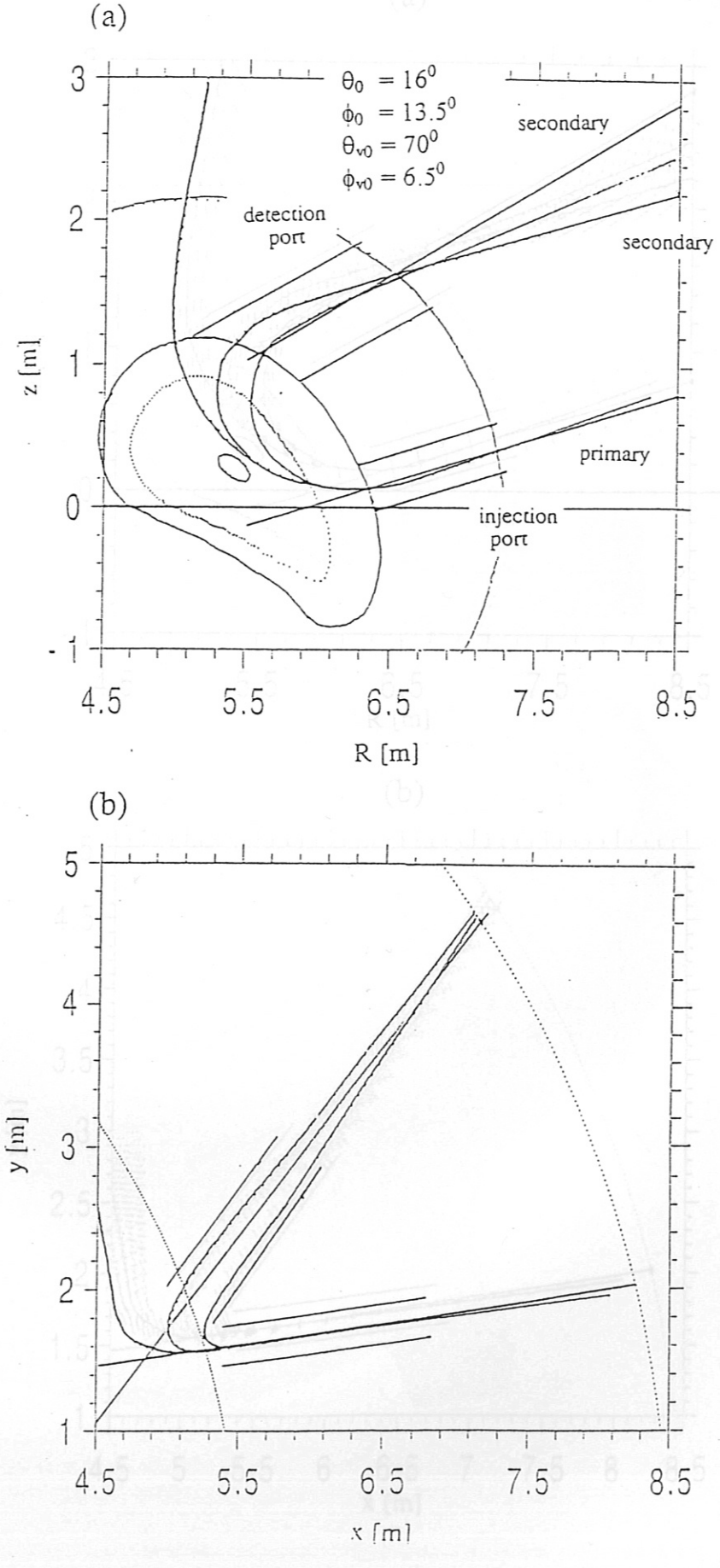
(a)
$\theta_0 = 16^0$
$\phi_0 = 13.5^0$
$\theta_{v0} = 70^0$
$\phi_{v0} = 6.5^0$
secondary
detection port
secondary
primary
injection port
z [m]
R [m]
(b)
y [m]
x [m]

Fig. 15.

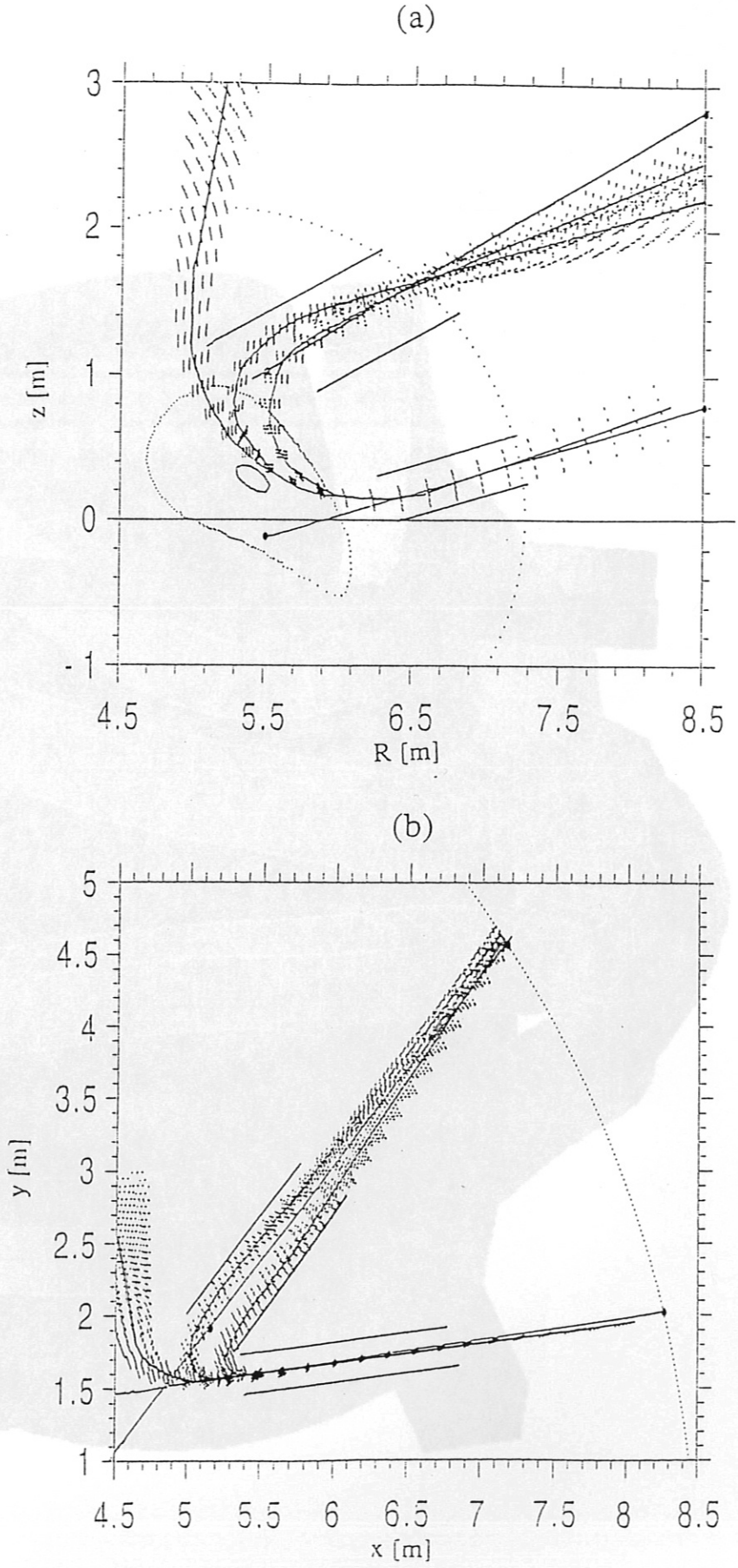
(a)
3
2
1
0
-1
z [m]
4.5
5.5
6.5
7.5
8.5
R [m]
(b)
5
4.5
4
3.5
3
2.5
2
1.5
1
y [m]
4.5
5
5.5
6
6.5
7
7.5
8
8.5
x [m]

Fig. 16a.

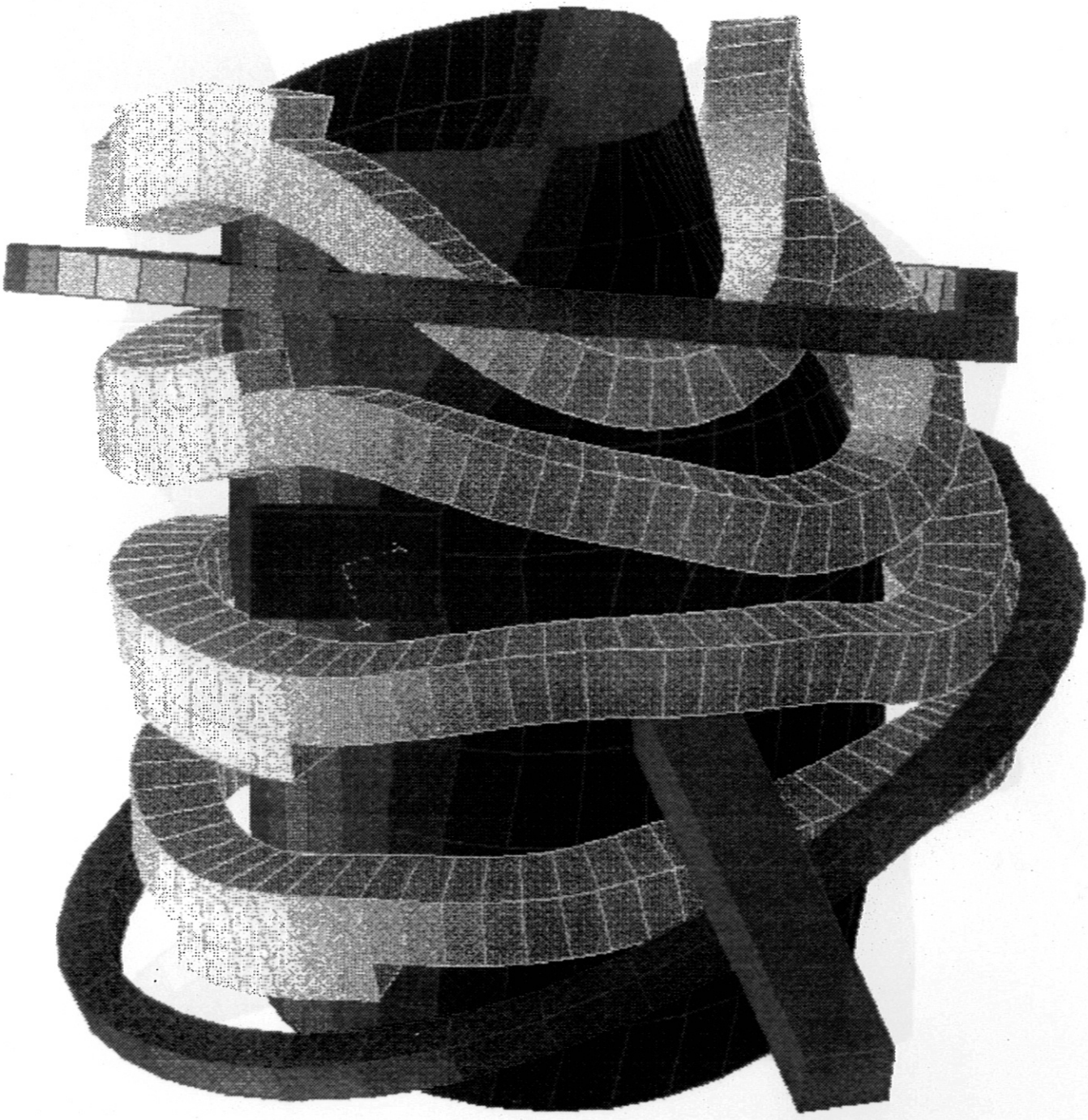

Fig. 16b.

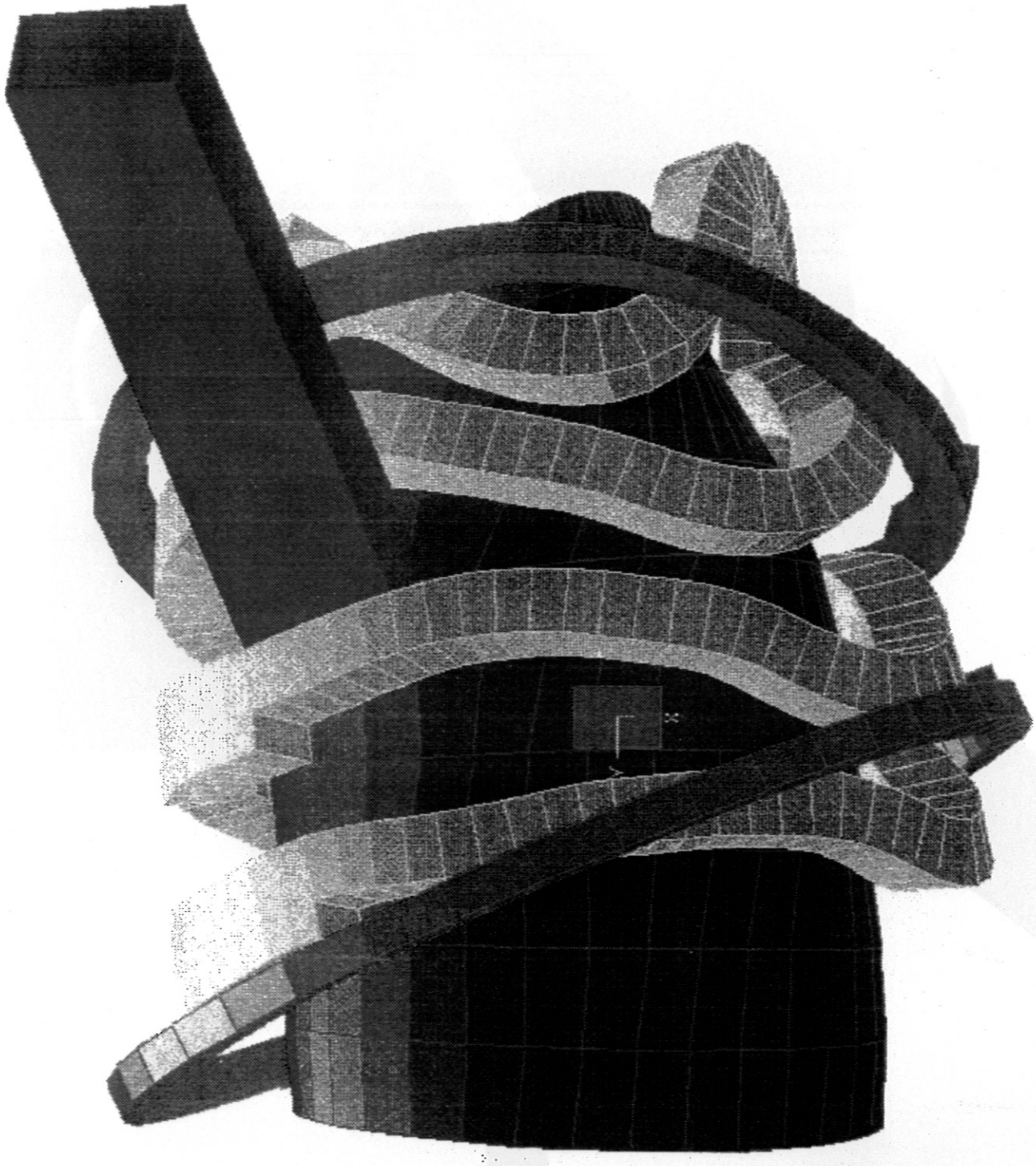

Fig. 16c.

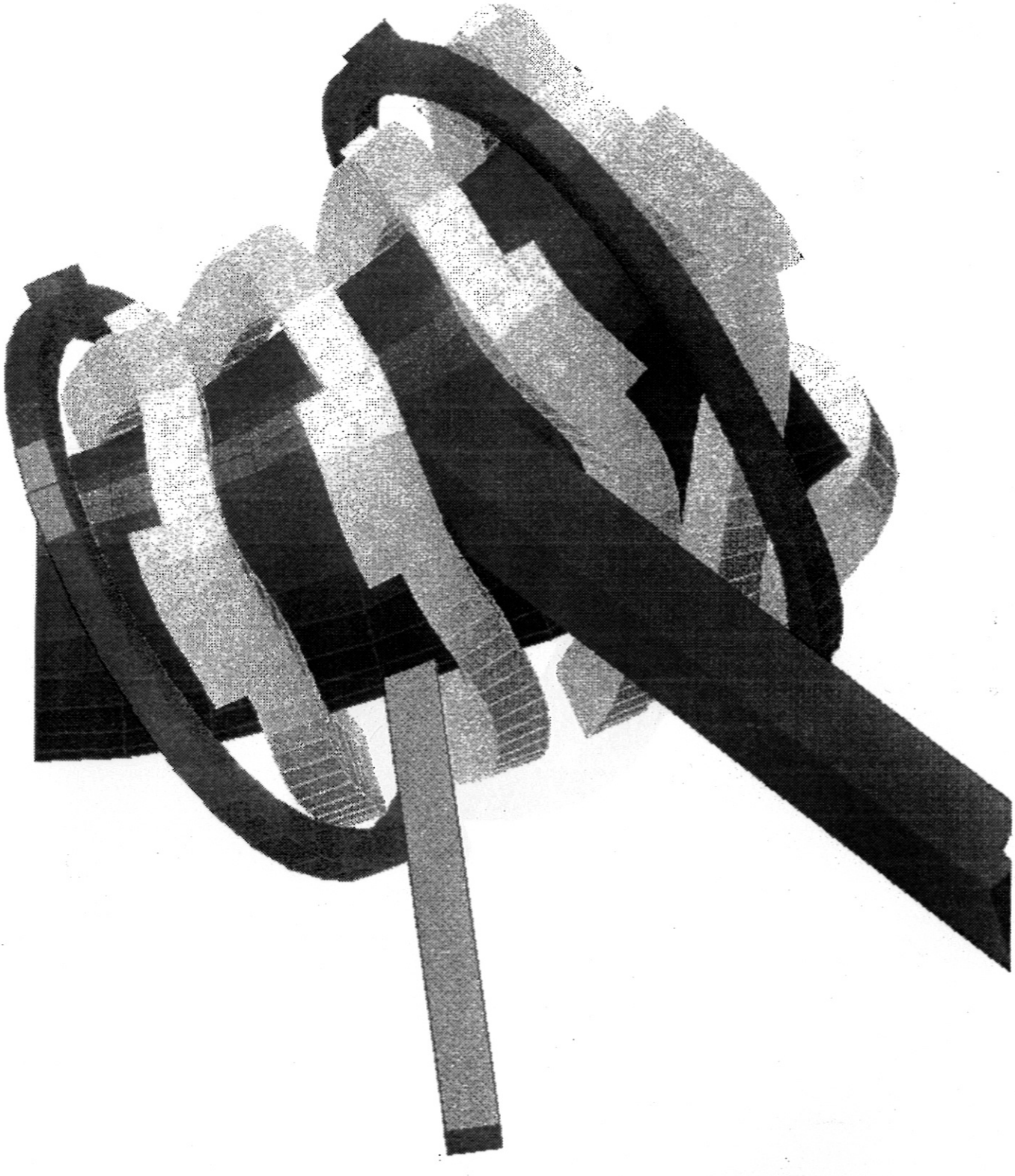

Fig. 17.